Lin *et al. Genome Medicine* (2026) 18:23
https://doi.org/10.1186/s13073-026-01604-2

Genome Medicine

RESEARCH Open Access

TiRank prioritizes phenotypic niches in tumor microenvironment for clinical biomarker discovery

Yuxiang Lin[1†], Zening Huang[2,3†], Ziyan Lin[4†], Yating Lin[1,5†], Jinsheng Song[4], Ling Luo[1], Jiayao Chi[4], Yeyang Zheng[4], Youxin Gao[2,3], Junjie Lin[1], Xinyu Li[4], Chenyu Liang[1], Lei Zhang[4], Xinkang Wang[1], Yuqin Sun[6*], Rongshan Yu[1,5*], Qiyue Chen[2,3*] and Mengsha Tong[1,4*]

Abstract

Background Tumor microenvironment (TME) plays a crucial role in cancer progression, metastasis, and treatment response. Recent advances in single-cell RNA sequencing (scRNA-seq) and spatial transcriptomics (ST) have provided valuable insights into the cellular diversity and spatial organization of the TME. However, prioritizing clinically relevant cellular subpopulations in spatial contexts using high-dimensional and sparse data remains a challenge.

Methods We introduce TiRank, a novel framework designed to prioritize clinically relevant spatial niches. TiRank incorporates a relative expression ordering (REO)-transformation module to mitigate systematic biases across modalities and utilizes a multitask transfer learning framework to align scRNA-seq, ST, and bulk transcriptomes into a unified embedding space. We benchmarked TiRank using multiple public datasets and pan-cancer clinical cohorts, demonstrating its capability to identify phenotypic cell subpopulations and spatial niches.

Results By integrating scRNA-seq, ST, and bulk transcriptomics with clinical phenotypes, TiRank demonstrates high accuracy in identifying drug-sensitive cells and clinically relevant spatial niches across various cancer types. As a case study, we applied TiRank to gastric cancer (GC) to prioritize spatial niches associated with patient outcomes. In our clinical cohort, TiRank successfully revealed a distinct spatial niche at the tumor boundary, characterized by an enrichment of cancer-associated fibroblasts (CAFs). This niche was associated with the efficacy of different treatment regimens. To validate this finding, we further performed multiplex protein imaging on an independent cohort to confirm the spatial distribution of the CAFs-enriched barrier. Moreover, this barrier, termed Fibro-Bar, was strongly

[†]Yuxiang Lin, Zening Huang, Ziyan Lin and Yating Lin contributed equally to this work.

*Correspondence:
Yuqin Sun
sunyuqin2017@163.com
Rongshan Yu
rsyu@xmu.edu.cn
Qiyue Chen
chenqiyue@fjmu.edu.cn
Mengsha Tong
mstong@xmu.edu.cn

Full list of author information is available at the end of the article

correlated with treatment response to neo-adjuvant chemoimmunotherapy. To improve accessibility, we developed TiRank as an open-source tool with an interactive graphical user interface for both researchers and clinicians.

Conclusions TiRank offers a phenotype-guided, cross-modal strategy to prioritize clinically relevant spatial niches by coupling an REO-based representation with transfer learning from bulk clinical cohorts. This design enables clinically supervised niche prioritization without requiring large, matched single-cell or spatial clinical cohorts, advancing biomarker discovery and supporting precision oncology.

Keywords Spatial transcriptomics, Tumor microenvironment, Clinically relevant spatial niches, Gastric cancer, Neo-adjuvant chemoimmunotherapy response

Background

The tumor microenvironment (TME) is a complex and dynamic ecosystem composed of both cancerous and non-cancerous cell populations. The cellular composition and spatial organization of the TME play important roles in tumor initiation, progression, metastasis, and therapeutic response [1–4]. Recent advancements in single-cell RNA sequencing (scRNA-seq) and spatial transcriptomics (ST) have offered profound insights into the cellular and spatial architectures that govern tumor biology, providing new opportunities to explore the roles of the TME in cancer [5–7]. Notably, combining spatial information from ST with molecular data has led to the discovery of tumor-associated structures, such as the tumor immune barrier in hepatocellular carcinoma [8] and the distinct accumulation of regulatory T cells around lymphatic vessels in colon cancer [9]. These studies highlight the importance of spatial niches in tumor progression and response to treatment. We defined spatial niches as the organizations of distinct cells, their co-localizations, interactions and neighboring relationships [10]. However, the roles of many spatial niches remain unclear, and their potential to predict prognosis and therapy response has yet to be fully explored. This underscores the need for advanced computational frameworks to identify clinically relevant subpopulations and spatial niches from scRNA-seq and ST data [11, 12].

Existing methods, such as unsupervised clustering algorithms like Seurat [13] and Scanpy [14], are widely used for identifying cellular clusters. These approaches depend on subjective clustering steps and are often suboptimal because the phenotypic subpopulations are usually not detected by standard clustering methods. Methods such as PENCIL [15] have been developed to identify phenotype-associated subpopulations directly from scRNA-seq data. However, these methods require large clinical cohorts to achieve the necessary statistical power, which can be costly and impractical in clinical settings [16]. Recently, Scissor [17], DEGAS [18] and scDEAL [19] leverage valuable clinical phenotypes from large public bulk transcriptomics [20]. These methods integrate scRNA-seq data with bulk transcriptomes to identify clinically relevant cellular subpopulations, even with a limited number of single-cell data. However, gene-expression-based integration strategies depend on consistent expression distributions across modalities, which is challenging due to systematic variations introduced by different techniques, particularly in bulk transcriptomics, scRNA-seq and ST [21, 22]. Moreover, they lack the ability to incorporate the spatial context provided by ST data, which is crucial for understanding tumor behavior and therapeutic responses. These methods primarily focus on scRNA-seq, limiting their ability to uncover clinically relevant spatial niches [23, 24].

To address these gaps, we introduce TiRank, a novel end-to-end toolkit that integrates scRNA-seq, ST, and bulk transcriptomes to prioritize clinically relevant spatial niches within the TME. TiRank comprises a relative expression ordering (REO)-transformation module that transforms the original gene expression matrix into a gene-pair matrix. This approach mitigates systematic biases between different transcriptomic modalities, improving computational efficiency and enhancing robustness across diverse datasets [25, 26]. Then, a multitask transfer learning framework is leveraged to align scRNA-seq, ST, and bulk transcriptomes into a low-dimensional embedding space, facilitating the identification of clinically relevant cell subpopulations and spatial niches.

In this study, we first validated TiRank's performance using multiple public benchmark datasets, demonstrating its superior performance in identifying drug-sensitive cells compared to existing methods. We then applied TiRank to pan-cancer clinical cohorts to identify prognostic cellular subpopulations and spatial niches, benchmarking its performance against established ground truths. To investigate the potential of TiRank in uncovering novel clinically relevant spatial niches, we further profiled the ST of patients with gastric cancer (GC), a cancer type for which predictive biomarkers for neo-adjuvant chemoimmunotherapy (NACI) response remain unclear. TiRank identified fibroblast-enriched subpopulations and immune cells at the tumor boundary, which were associated with distinct treatment regimens. Further validation using imaging mass cytometry (IMC) on an independent cohort of GC patients confirmed the spatial distribution

of a fibroblast-enriched barrier, termed Fibro-Bar. We found that the Fibro-Bar was negatively correlated with tumor regression grade (TRG), which may serve as a predictive biomarker to guide NACI treatment strategies.

Methods

TiRank framework

Step1. Phenotypic gene-pair matrix construction

We group the phenotype information from bulk transcriptomes into three categories: survival records (e.g. overall survival), binary labels (e.g., response vs. non-response), and continuous values (e.g., IC-50 values). For each category, we apply the corresponding statistical method to select phenotypic genes. Cox regression is used for survival records, Student's t-test is for binary labels and Pearson correlation is for continuous values. Specifically, we identify positive genes G_p, and negative genes G_n according to the following criteria:

$$G_p = \{g \mid p \leq p' \cap \left[\mathbb{1}_{\{Cox\}}\left(HR > 1\right) \vee \mathbb{1}_{\{Cls\}}\left(\mu_0 > \mu_1\right) \vee \mathbb{1}_{\{Reg\}}\left(r > 0\right)\right]\};$$

$$G_n = \{g \mid p \leq p' \cap \left[\mathbb{1}_{\{Cox\}}\left(HR < 1\right) \vee \mathbb{1}_{\{Cls\}}\left(\mu_0 < \mu_1\right) \vee \mathbb{1}_{\{Reg\}}\left(r < 0\right)\right]\},$$

g represents a gene, p is *p*-value, and *p'* is the significance level (the default value is 0.05). HR is the hazard ratio from Cox regression (*Cox*), μ_0 and μ_1 are mean expression values in two classes for classification (*Cls*). r is the correlation coefficient for regression (*Reg*). The indicator function $1_{\{Mode\}}(\bullet)$ specifies the statistic method.

Subsequently, we construct PGPs based on the gene sets G_p and G_n. The REO of a gene pair (g_a, g_b) is defined as:

$$REO\left(g_a, g_b\right) = \begin{cases} 1, \ if \ E(a) > E(b) \\ -1, \ if \ E(a) < E(b) \end{cases},$$

where $g_a \in G_p$, $g_b \in G_n$ and $E(g)$ denotes the expression value of gene g.

We transform the original expression profile into a binary gene-pair matrix and define it as the PGP matrix. This transformation reduces feature redundancy and bridges the gap between different data modalities. These PGP matrices are then used for model training (Step 2).

Step2. Model training and multitask loss functions

Based on the PGP matrix, we leverage a three-layer MLP as an encoder to project original features into embedding space guided by tailored multitask learning objectives. The encoding procedure is defined as:

$$\mathrm{X}_{emb} = ELU\left(X^{\mathrm{T}}\theta_{emb} + \mathrm{b}_{emb}\right).$$

Here, $\mathbf{X}_{emb}$ represents the embedding of the input PGP matrix $\mathbf{X}$ from bulk transcriptomics, scRNA-seq, or spatial transcriptomics data. The matrices $\boldsymbol{\theta}_{emb}$ and $\mathbf{b}_{\mathrm{emb}}$ are the learnable parameters and bias term, respectively.

Subsequently, an alternative three-layer MLP is employed to predict the TiRank score, which indicates the association between individual cells (or spots) and the phenotype:

$$TiRank\ Score\left(\mathrm{X}\right) = A\left(\mathrm{X}_{emb}^{T}\theta_{pred} + \mathrm{b}_{pred}\right),$$

the $TiRankScore(\mathbf{X})$ denotes the TiRank score of the input PGP matrix, and $\boldsymbol{\theta}_{pred}$ and $\mathbf{b}_{pred}$ are the trainable parameters and bias term for TiRank score predicting, respectively. The function $A(\bullet)$ is the activation function that constrains the output TiRank score within an appropriate range. Specifically, $\mathrm{sigmoid}(\bullet)$ is applied for survival prediction, while $\mathrm{softmax}(\bullet)$ is used for binary labels and continuous variables.

To guide the model in constructing informative embeddings and efficiently predicting scores, we leverage a multitask learning objective. The overall optimization target is defined as:

$$\mathrm{L} = \lambda_0 ||\theta_{emb}||_1 + \lambda_1 L_{Bulk} + \lambda_2 L_{regular}.$$

This total loss L comprises three independent parts, balanced by hyperparameters λ_0, λ_1 and λ_2. $||\theta_{emb}||_1$ is the L1-norm regularization term that highlights important gene pairs for prediction. $\mathrm{L}_{\mathrm{Bulk}}$ denotes the deviation between the TiRank score and the given phenotype label in bulk transcriptomics, considered as ground truth. Specifically, we tailored the $\mathrm{L}_{\mathrm{Bulk}}$ to accommodate distinct input phenotypes. For survival data, we utilized survival time and event indicators (t, e) to denote the survival time and event status. We defined the set P, which includes all patient pairs (i, j) that satisfy two conditions: both events occurred (e_i=e_j=1) and the survival time of patient i precedes that of patient j ($t_i < t_j$). We employed the Cox partial log-likelihood (CPL) loss, expressed as follows:

$$L_{Bulk-Cox} = \frac{1}{|P|}\sum\nolimits_{(i,j)\in P} log(1 + e^{(1+e^{-(\widehat{y}_i - \widehat{y}_j - m)})}),$$

where $\widehat{y}_i$ represents the TiRank score of patient i, and m denotes the margin parameter (default = 0.1). For discrete and continuous data, we utilized the cross-entropy loss (CE) and mean-squared error (MSE), represented by the following formulas:

$$L_{Bulk-Cls} = -\frac{1}{N}\sum\nolimits_{i=1}^{N}\sum\nolimits_{c=1}^{C} y_{i,c} log\left(\widehat{y}_{i,c}\right);$$

$$L_{Bulk-Reg} = \frac{1}{N}\sum_{i=1}^{N}(y_i - \widehat{y}_i)^2,$$

In these formulas, N denotes the number of patients in the bulk transcriptomics dataset, y_i represents the true label or value of the given sample, and c corresponds to the true category label in the classification task. Consequently, for bulk transcriptomes, the model outputs a single continuous score per sample $S \in [0,1]$, which is directly optimized against the bulk phenotype via the specified supervised loss.

The regularization term $\mathrm{L_{regular}}$ is designed to embed individual cells or spots while preserving the similarity of transcriptional patterns or spatial locations. We tailor $\mathrm{L_{regular}}$ for both scRNA-seq and ST data.

For single cell transcriptomics, the regularization constrains cells with similar transcriptional patterns to be projected closely in the embedding space, as defined by:

$$L_{\mathrm{regular-sc}} = 1 - \frac{\sum_{i,j} A_{ij} B_{ij}}{\sqrt{\sum_{i,j} A_{ij}^2}\sqrt{\sum_{i,j} B_{ij}^2}}.$$

Here, A_{ij} is the shared nearest neighbor (SNN) graph calculated through Scanpy package to determine cells with similar expression patterns, and B_{ij} is the inner product of the embedding matrix $\mathbf{X}_{emb}$, representing the similarity between individual cells.

For spatial transcriptomics, we developed a whole slide image (WSI)-guided spatial location-aware module to ensure that spots with similar spatial locations are projected nearby in the latent space. We hypothesize that regions with similar features on hematoxylin and eosin (H&E)-stained slides are likely to have similar phenotype-associated labels. Initially, we mapped each spot to its corresponding H&E patch using the following formula:

$$x_{(i,j)} = \begin{bmatrix} a_{(i-\frac{l}{2},j-\frac{l}{2})} & \cdots & a_{(i-\frac{l}{2},j+\frac{l}{2})} \\ \vdots & \ddots & \vdots \\ a_{(i+\frac{l}{2},j-\frac{l}{2})} & \cdots & a_{(i+\frac{l}{2},j+\frac{l}{2})} \end{bmatrix}.$$

In this formula, i and j denote the spatial coordinates of spot x in the image, $a_{(i,j)}$ represents the pixel values in the RGB channels at position (i, j), and l is the edge length of the square patch. For our study, we assigned H&E patches of 50×50 pixels to each spot [27]. Subsequently, we employed CTransPath, a pretrained model trained on a large dataset of WSIs from various public databases using contrastive learning [28]. This model extracts features from the H&E patches. We then applied unsupervised clustering using the k-means algorithm to categorize these H&E patches into k (default k=8) distinct regional clusters. An additional MLP was utilized to allocate the spatial cluster category of each spot based on the embeddings derived from the PGP of ST data. The loss is defined as follows:

$$L_{\mathrm{regular-st}} = -\frac{1}{N}\sum_{i=1}^{N}\sum_{c=1}^{k} y_{i,c} log\left(\widehat{y}_i\right);$$

$$\widehat{y}_i = argmax\left(softmax\left(\boldsymbol{X}_{emb}^{T}\boldsymbol{\theta}_{regular-st} + \boldsymbol{b}_{regular-st}\right)\right).$$

In these equations, $\widehat{y}_i$ denotes the predicted spatial cluster label of each spot, and N represents the number of spots within the spatial transcriptomics dataset. This step constrains the input spatial transcriptomic data to be embedded into a latent space that preserves spatial information.

Step3. GMM-based filter module

After assigning TiRank scores to individual cells or spots, we introduce a rejection module to filter out cells or spots that are weakly associated with the given phenotype, particularly in survival and discrete category predictions. We fit a three-component GMM [29], an unsupervised method for distinguishing independent normal distributions within a mixed Gaussian distribution, on the bulk-sample TiRank scores only to expose three regimes in the score distribution: a positive (favorable phenotype-associated) mode, a negative (adverse-phenotype-associated) mode, and a diffuse middle region. The GMM models the probability distribution of the TiRank scores as:

$$p(S) = \sum_{k=1}^{3}\pi_k \mathcal{N}\left(TiRankcore|\mu_k, \sigma_k^2\right),$$

wherein $p(S)$ represents the probability density for a given score, π_k denotes the mixing coefficient for the k^{th} Gaussian component, and μ_k and σ_k^2 are the mean and variance of that component's Gaussian distribution, respectively.Once the GMM model is fitted, each cell or spot, initially assigned a continuous TiRank Score, is assigned a discrete TiRank Label (TiRank$^+$, TiRank$^-$, or Background) as follows:

$$TiRank\ Label(i) = \begin{cases} 0, & if\ |TiRank\ Score(i) - \mu_0| \le T \\ 1, & if\ |TiRank\ Score(i) - \mu_1| \le T. \\ Background & others \end{cases}$$

Here, i represents an individual cell or spot, μ_0 and μ_1 are the lowest and the highest component means of GMM respectively, and T (default = 0.05) is the predefined classification threshold. The selection of a GMM is methodologically appropriate, as the TiRank Scores are constrained to the $[0,1]$ interval, with phenotype-associated scores expected to cluster near the boundaries, whereas phenotype-independent scores are assumed to be more diffusely distributed. By convention, for

drug response tasks, TiRank Label "0" (TiRank$^-$) corresponds to a 'responsive' phenotype, while TiRank Label "1" (TiRank$^+$) indicates a 'resistant' phenotype. Similarly, for prognostic tasks, TiRank Label "0" typically signifies favorable prognosis, whereas TiRank Label "1" corresponds to poor prognosis. The resulting TiRank Scores and discrete TiRank Labels are subsequently utilized for the identification of phenotype-associated cell subpopulations or spatial niches, or for other direct downstream analyses.

Identification of clinically relevant cell subpopulations and spatial niches

With the TiRank Scores and TiRank Labels for individual cells or spots, we further identify clinically relevant cell subpopulations or spatial niches. We adopt a permutation test to measure the significance of enrichment of phenotype-associated cells or spots within given cellular subpopulations or spatial niches. Specifically, we first create a null distribution by repeatedly randomizing phenotype labels across individual identities. In each permutation, we recalculate the number of phenotype-associated cells or spots within the given subpopulation or niche. The statistical significance for each cluster is determined by calculating the proportion of permutations where the permuted label counts exceed the observed label count in the actual data. The calculation procedure is as follows:

$$p = \begin{cases} 1, & C_{obs} = 0 \\ \frac{\sum_{i=1}^{n} [C_{perm} \geq C_{obs}] + 1}{n+1}, & otherwise \end{cases}.$$

Here, p is the p-value for the cluster, C_{obs} is the observed number of phenotype-associated cells or spots within the cluster, C_{perm} represents the number of phenotype-associated cells or spots within the cluster in the i^{th} permutation, and n is the total number of permutations. A cluster with a p-value less than 0.05 is considered a phenotype-associated cell subpopulation or spatial niche.

TiRank model implementation and hyperparameter optimization

The TiRank model was implemented using the Adam optimizer for gradient-based optimization and "StepLR" for learning rate scheduling. A clear distinction was maintained between the training and inference phases, and a separate, task-specific model was trained for each clinical task.

Training and validation phase

For each task, the model was trained exclusively on the corresponding bulk transcriptomic data, which contains the clinical phenotype labels (e.g., survival, drug response). To optimize hyperparameters (e.g., learning rate α, number of training epochs, and loss coefficients λ), we employed Optuna [30] and partitioned the bulk transcriptomic data into a training set (85%) and a validation set (15%). All processes, including data sampling, feature selection (PGP construction), and model training, were conducted on the training set. The validation set was used to select the final hyperparameters that achieved the lowest loss and best predictive performance on unseen bulk data.

Inference and evaluation phasex

After a task-specific model was finalized and trained on the entire bulk dataset using the selected hyperparameters, it was applied to the corresponding scRNA-seq or ST datasets to obtain per-cell/per-spot TiRank scores. The model, guided by the PGP features, projected the single cells or spatial spots into the learned phenotypic embedding space to generate TiRank scores. For binary reporting in drug-response tasks, we classify cells/spots using the bulk-fitted GMM parameters (μ_0, μ_1 and T) as described in Step 3. The ground-truth labels associated with the scRNA-seq or ST data (e.g., cell line drug sensitivity) were not used during training and were reserved only for the final performance evaluation and benchmarking.

Data sampling in TiRank

In bulk transcriptome datasets with survival information or binary labels, an imbalance in the number of different groups could impact model performance. To address this, we employed synthetic minority over-sampling technique (SMOTE) [31] to balance the proportions of the two groups during model training. The use of SMOTE enables the model to effectively learn the characteristics of minority groups, thereby reducing the likelihood of overfitting and increasing robustness.

Benchmarking of TiRank and comparison to other methods in cell line data

Benchmark design and splits

We displayed the performance of TiRank in drug response prediction, compared with three existing methods: Scissor [17], DEGAS [18] and Beyondcell [32]. Ten bulk transcriptomics datasets and five scRNA-seq with true response labels were used to benchmark. For each drug, each method was trained only on bulk transcriptomes annotated with lg (IC50)/drug-response labels (GDSC/CCLE). After training converges, the fixed model is applied to scRNA-seq cell-line datasets for inference to the per-cell association. Ground-truth single-cell drug labels (where available) are used only for evaluation of the performance, which were not used in training.

Metrics and execution

The comparisons were conducted using three metrics, accuracy, F1-score and time consumption:

Accuracy represents the ability of the model to correctly predict labels among all predictions:

$$\text{Accuracy} = \frac{\text{TP} + \text{TN}}{\text{TP} + \text{TN} + \text{FP} + \text{FN}}$$

where the TP and TN indicate the true positive and true negative, while FP and FN represent the false positive and false negative.

F1-score can be interpreted as a weighted average of precision and recall. F1-score reaches its highest value at 1 and lowest score at 0. The equation for the F1-score is:

$$\text{F1-score} = \frac{2 * \text{TP}}{2 * \text{TP} + \text{TN} + \text{FP}}$$

Precision can be interpreted as the proportion of true positive predictions among all positive predictions made by the model. Precision reaches its highest value at 1 and lowest score at 0. The equation for precision is:

$$\text{Precision} = \frac{\text{TP}}{\text{TP} + \text{FP}}.$$

Recall can be interpreted as the proportion of true positive predictions among all actual positive cases. Recall reaches its highest value at 1 and lowest score at 0. The equation for recall is:

$$\text{Recall} = \frac{\text{TP}}{\text{TP} + \text{FN}}$$

Time consumption

All methods were executed on a Linux server equipped with 32 CPUs and 256 GB of RAM. For methods supporting GPU acceleration (TiRank and DEGAS), an NVIDIA GeForce GTX 1080 with 8 GB of memory was utilized.

Public transcriptomics dataset with clinical phenotypes

To evaluate the performance of TiRank in identifying key cellular subpopulations associated with clinical drug response and prognosis, we collected and preprocessed public datasets including 46 bulk transcriptomic, 11 scRNA-seq, and 3 ST. Detailed metadata for all datasets, including study identifiers, cancer types, data modalities, platforms, cohort sizes, and treatment information, are provided in Additional file 2: Table S1. These datasets include six cancer types: melanoma, LUAD, HCC, GC, CRC and AML. The clinical information included drug response, overall survival, disease specific survival and recurrence free survival. More details about the preprocessing procedures are provided in the Supplementary Methods.

Systematic review of cellular subpopulations and spatial niches in cancer

To investigate the clinical significance of cellular subpopulations and spatial niches across various cancers, we conducted a systematic literature review (Additional file 2: Table S2). Using PubMed (https://pubmed.ncbi.nlm.nih.gov/), we retrieved high-quality research articles focusing on diverse cancer types. Each article was meticulously evaluated to identify content related to cellular subpopulations or spatial niches, defined as specific cellular subtypes or spatial structures (e.g., niches, region hubs, buds, barriers, nests, co-location, or cell–cell interactions) quoted directly from the " Results" section, and their associations with clinical phenotypes, such as survival outcomes, treatment response, metastasis, immunosuppression, or tumor progression.

Relevant articles were further analyzed to extract direct quotes describing these subpopulations or structures, their linked phenotypes, and supporting evidence. Phenotype evidence consisted of sentences explicitly connecting spatial niches or subpopulations to clinical outcomes, while experimental evidence included sentences validating these phenotypes through molecular biology experiments. Extracted data, including article details, cancer types, identified subpopulations or niches, associated phenotypes, and experimental validations, were compiled into a summary table (Additional file 2: Table S2). This dataset facilitated the validation of algorithms like TiRank for identifying clinically significant cellular subpopulations and spatial niches, with all findings cross-referenced by PMID.

Evaluation of algorithms for predicting phenotype-associated cellular subpopulations in single-cell transcriptomics

Benchmark design

To evaluate the performance of algorithms in predicting associations between bulk transcriptomics and scRNA-seq datasets with same phenotypes, as well as identifying phenotype-associated cell subpopulations, the following protocol was used. For each cancer type, the model was trained using the prognosis labels (e.g., Overall Survival) from the bulk transcriptomics data only (L_Bulk for TiRank). The scRNA-seq expression data was used in an unsupervised manner ($L_regular - sc$).

Ground truths and aggregation

We employed three metrics: precision, false rate, and coverage. These metrics were computed based on the algorithm's predictions compared to established ground

truth data, with predictions classified as 'unknown' or 'background' excluded from the calculations. Below, we define each metric, provide their respective formulas.

Precision measures the accuracy of the algorithm's positive predictions, specifically the proportion of correctly predicted associations among all positive predictions made by the algorithm. In standard terms, precision is defined as:

$$\text{Precision} = \frac{\text{TP}}{\text{TP} + \text{FP}},$$

TP (true positives) represents the number of bulk transcriptomics-scRNA-seq pairs correctly predicted as associated with the phenotype, while FP (false positives) indicates the number of pairs incorrectly predicted as associated. A high precision suggests that the algorithm's positive predictions are reliable.

False rate quantifies the proportion of incorrect positive predictions among all positive predictions. It is the complement of precision and is calculated as:

$$\text{False Rate} = \frac{\text{FP}}{\text{TP} + \text{FP}},$$

this metric highlights the frequency of errors in the algorithm's positive predictions, with a lower false rate indicating fewer mistaken associations.

Coverage assesses the ability of the algorithm to identify cell subpopulations associated with the phenotype across all pairs. Unlike standard recall, which focuses on true positives relative to all actual positives, coverage is a custom metric defined here as the average proportion of subpopulations predicted as associated within each pair. It is expressed as:

$$Coverage = \frac{1}{|P|}\sum\nolimits_{p \in P} \frac{|A_p|}{|S_P|},$$

where, P denotes the set of pairs with predictions, S_p is the set of all subpopulations within a pair p, and A_p is the subset of subpopulations predicted as associated. Coverage reflects the breadth of the algorithm's predictions across subpopulations.

Evaluation of algorithms for predicting phenotypic niches in spatial transcriptomics data

To evaluate the performance of multiple algorithms in predicting phenotype-associated spatial niches, we utilized three spatial transcriptomics cohorts: two public and one private, each addressing a distinct clinical problem. The first cohort, comprising four slides from CRC patients with different consensus molecular subtypes (CMS) as described by Valdeolivas et al., includes spots manually annotated by pathologists to identify immune-aggregate niches. The second cohort, from Wu et al., investigates the association between high $CD8^+$ T cell infiltration and the response to ICB treatment following neo-adjuvant chemotherapy, where the algorithms were applied to identify spatial niches characterized by elevated $CD8^+$ T cell infiltration. The third cohort, a private dataset from nine GC patients, features annotations of TLS on spatial transcriptomics slides, with the algorithms used to detect regions enriched with TLS.

We assessed the performance of each algorithm at the single-spot level using five metrics: precision, recall, F1-score, balanced accuracy, and Jaccard index. The formulas for balanced accuracy and Jaccard index are provided as follows:

$$\text{Balanced Accuracy} = \frac{1}{2}\left(\frac{\text{TP}}{\text{TP} + \text{FN}} + \frac{\text{TN}}{\text{TN} + \text{FP}}\right);$$

$$\text{Jaccard Index} = \frac{\text{TP}}{\text{TP} + \text{FP} + \text{FN}},$$

where TP denotes the number of spots with true positives, FP the number of false positives, the number of true negatives, and FN the number of false negatives.

Collection of clinical cohorts for GC

We collected three clinical cohorts of GC patients from the Fujian Medical University Union Hospital and Zhangzhou Affiliated Hospital of Fujian Medical University. These cohorts were used to construct the UnionH datasets: UnionH-1, UnionH-2 and UnionH-3. The UnionH-1 cohort included 50 GC patients receiving NACI, which were collected from the Fujian Medical University Union Hospital from February 2022 to March 2024.

This cohort was used for bulk gene expression profiling. The UnionH-2 cohort consisted of 9 treatment-naïve GC patients (Additional file 2: Table S3). These patients were from the Fujian Medical University Union Hospital from January 2022 to December 2023. This cohort was used to perform spatial transcriptome analysis. The UnionH-3 cohort involved 10 GC patients who underwent gastroscopy followed by NACI to reduce tumor size, with subsequent surgical resection (Additional file 2: Table S4). These gastroscopic specimens were from the Department of Gastrointestinal Surgery, Zhangzhou Affiliated Hospital of Fujian Medical University from August 2021 to February 2023. Tumor samples from gastroscopy in this cohort were analyzed using IMC.

The inclusion criteria for patients were as follows: (a) histological diagnosis of GC; (b) available follow-up data and clinicopathological features; (c) TNM staging was performed according to the 8th edition American Joint Committee on Cancer (AJCC) guidelines. The exclusion

criteria included non-formalin-fixed tumor center, paraffin-embedded tumor specimen (CT), and invasive margin (IM) at initial diagnosis. The UnionH-1 and UnionH-2 cohort were approved by the Ethics Committee of Fujian Medical University Union Hospital (Ethical approval No. 2020YF013). The Cohort UnionH-3 was approved by the Ethics Committee of Zhangzhou Affiliated Hospital of Fujian Medical University (Ethical approval No. 2023LWB046). All procedures complied with the ethical standards of the Declaration of Helsinki. All patients whose tissue samples were used in this study signed informed consent.

Bulk transcriptomics of UnionH-1 cohort

Sequencing

Total RNA was extracted from GC samples using TRIzol Reagent (Invitrogen, Cat. No. 15596026) following the method described by Chomczynski et al. [33]. DNA digestion was carried out using DNase I to remove genomic DNA contamination. RNA quality was assessed by measuring the A260/A280 ratio using a NanodropTM OneC Spectrophotometer (Thermo Fisher Scientific, Inc.), and RNA integrity was confirmed via 1.5% agarose gel electrophoresis. RNA quantity was determined using a Qubit 3.0 Fluorometer with the QubitTM RNA Broad Range Assay Kit (Life Technologies, Q10210). For RNA-seq library preparation, 2 μg of total RNA was used to generate stranded RNA libraries using the KC-DigitalTM Stranded mRNA Library Prep Kit for Illumina® (Catalog No. DR08502, Wuhan Seqhealth Co., Ltd., China), following the manufacturer's instructions. The kit incorporates unique molecular identifiers (UMIs) to label pre-amplified cDNA molecules, thereby eliminating duplication bias during PCR amplification and sequencing. Libraries corresponding to fragment sizes between 200 and 500 bp were selected, quantified, and then sequenced using the Illumina NovaSeq 6000 platform with a paired-end 150 bp (PE150) configuration.

Data analysis

Raw sequencing data were initially processed using Trimmomatic (version 0.36) to remove low-quality reads and adapter sequences. Clean reads were then further processed using custom scripts to eliminate any duplication bias introduced during library preparation and sequencing. Specifically, clean reads were clustered according to their UMI sequences, grouping reads with identical UMIs into the same cluster. Reads within each cluster were compared by pairwise alignment, and clusters with over 95% sequence identity were merged into new sub-clusters. After sub-cluster generation, multiple sequence alignment was performed to obtain a consensus sequence for each sub-cluster, effectively eliminating errors and biases introduced by PCR amplification or sequencing. The deduplicated consensus sequences were then used for downstream RNA-seq analysis. These sequences were mapped to the human reference genome (GRCh38) and STAR software (version 2.5.3a) was applied with default parameters. Reads mapped to the exonic regions of each gene were quantified using featureCounts (Subread v1.5.1; Bioconductor), and RPKM values were calculated to normalize gene expression levels for gene length and sequencing depth.

10 × visium spatial transcriptomics of UnionH-2 cohort

Sample collection and sequencing

GC samples were collected and processed as described above. RNA quality of FFPE tissue blocks was assessed by calculating the DV200 value of RNA extracted using the Qiagen RNeasy FFPE Kit, according to the manufacturer's protocol. After the Tissue Adhesion Test, 5 μm sections were cut and mounted onto Visium Spatial Gene Expression Slides (10 × Genomics, Pleasanton, CA, USA) following the Visium Spatial Protocols-Tissue Preparation Guide (10 × Genomics, CG000408 Rev A). The slides were then air-dried overnight and incubated at 60 °C for 2 h to promote optimal tissue adhesion. Deparaffinization was performed following the Visium Spatial FFPE Deparaffinization, H&E Staining, Imaging & Decrosslinking Protocol (10 × Genomics, CG000409 Rev A). Tissue sections were stained with hematoxylin and eosin and imaged at 20 × magnification using a Leica Aperio Versa8 whole-slide scanner (Leica Microsystems, Wetzlar, Germany). Following imaging, decrosslinking was performed, and human whole transcriptome probe panels were added to the tissue sections. The probe pairs hybridized to their target genes, and ligation products were released by RNase treatment and tissue permeabilization. The ligated probes were then hybridized to the spatially barcoded oligonucleotides present in the capture areas. Spatial Transcriptomics libraries were generated from the ligated probes and subsequently sequenced on the Illumina NovaSeq 6000 system (Illumina, Inc., San Diego, CA, USA), with sequencing performed by Beijing Novogene Technology Co., Ltd.

Data processing

After cDNA library construction and sequencing, raw FASTQ files were processed using Space Ranger v1.3.0 (10 × Genomics) for probe alignment to the GRCh38. Histology images were aligned using the fiducial markers, and the filtered count matrix was used for downstream analysis.

Defining pathological regions within spatial transcriptome

We used the Cottrazm package [34] to identify malignant tumor regions and tumor boundaries in each tissue slice. Based on these results, we defined pathological regions

by cross-referencing them with hematoxylin and eosin (H&E) staining and annotations provided by experienced pathologists.

Entropy calculation

We characterized the heterogeneity of regions by calculating their entropy levels. Metadata from nine gastric cancer tissue slices were integrated to determine the probabilities of therapy response labels. This was achieved by calculating the ratio of each label's occurrence to the total number of labels in the pathological annotations. The entropy values $\mathrm{H(X)}$ for the regions were then calculated using the following formula:

$$\mathrm{H}\left(\mathrm{X}\right) = -\sum_{i=1}^{n} p\left(x_i\right) log_2 p\left(x_i\right),$$

where $\mathrm{p}(x_i)$ represents the probabilities of therapy response labels. We hypothesize that regions with higher entropy values may have greater predictive significance for therapy outcomes.

Deconvolution and spatial co-localization of cellular subpopulations in ST

To analyze the spatial co-localization of cellular subpopulations within ST data, we employed two R packages: CARD [35] and MISTy [36]. First, CARD takes scRNA-seq data annotated with cell types and ST data as inputs, resulting in cell fractions for each spot. Subsequently, CARD calculates the Spearman correlation between pairs of cellular subpopulations to assess their co-localization within individual spots. Additionally, MISTy utilizes linear regression and random forest to identify the most significant factors, such as cell type fractions, gene expression, or pathway activities, that contribute to the prediction of target cellular subpopulations.

Antibody conjugation and validation for imaging mass cytometry

A panel comprising 35 proteins, including immune markers, cancer-associated fibroblasts, and other non-immune proteins, was developed to distinguish between various cell types and states. Additional file 2: Table S5 details the antibodies and corresponding metals employed in this study. Antibodies were procured as follows: 28 from Abcam (https://www.abcam.com/), three from Fl uidigm (https://www.fluidigm. com), and the remaining five from MERCK (https://www.merck.com/) and CST (https://www.cellsignal.cn/). For the conjugation of unla beled antibodies with metals, the Maxpar X8 Multimetal Labeling Kit (Fluidigm, Catalog No. 201300) was utilized in accordance with the manufacturer's instructions. The titration and specificity of the conjugated antibodies were evaluated by visually comparing IMC images of select tissue slides from GC patients.

Preparation and staining of tissue slide for IMC in UnionH-3 cohort

To stain the tissue slides, the IMC staining protocol (Fluidigm, PN400322) provided by Fluidigm was followed. FFPE tumor samples were heated at 65 °C for 2 h to remove all visible wax. Subsequently, the slides were deparaffinized twice in fresh xylene for 10 min each and then rehydrated using a graded alcohol series (100%, 95%, 80%, and 70% for 5 min each). Antigen retrieval was achieved by immersing the slides in Tris–EDTA buffer (pH 9.0) within a 96 °C water bath for 30 min. After cooling to 70 °C, the slides were blocked with 3% bovine serum albumin (BSA) in phosphate-buffered saline (PBS, Maxpar) for 45 min in a hydration chamber at room temperature. Concurrently, the antibody cocktail was prepared in a 0.5% BSA buffer at the optimal dilution for each antibody. Following the blocking step, the slides were incubated with the antibody cocktail overnight at 4 °C in a hydration chamber. The next day, the slides were washed twice with 0.2% Triton X-100 in PBS (Maxpar), followed by two washes with PBS (Maxpar). For DNA staining, the slides were treated with Intercalator-Ir (Fluidigm, Catalog No. 201192 A) in PBS (Maxpar) at room temperature for 30 min. Finally, the slides were washed twice with deionized water and air-dried for at least 20 min before imaging mass cytometry acquisition.

Imaging mass cytometry

Images were acquired using the Hyperion Imaging System (Fluidigm) in accordance with the manufacturer's protocol. To select the regions for Imaging Mass Cytometry (IMC) examination, we collaborated with a professional pathologist, who utilized hematoxylin and eosin (H&E)-stained serial tissue sections to randomly identify ROIs from gastroscopic samples across different patients, resulting in a total of 61 images (Additional file 2: Table S6). Image capture was performed via laser ablation at a frequency of 200 Hz, and raw data were obtained using commercial acquisition software associated with the Hyperion Imaging System (Fluidigm). The operational state of the Hyperion Imaging System was monitored by interspersing data acquisition with a tuning slide (Fluidigm).

Cell segmentation, protein quantification, and normalization

We first assessed the quality of each image by meticulously inspecting all marker staining patterns using the MCD Viewer (Fluidigm, v1.0.560.6). Subsequently, the standard IMC pre-processing procedures, including

image extraction, normalization, cell segmentation, and protein quantification [37], were performed. The segmentation process utilized the Mesmer algorithm, implemented in the DeepCell package [38], which segments cells in a fully automated manner based on pretrained neural networks. Following segmentation, we obtained the expression levels of each cell within the images. To mitigate noise signals, arcsine transformation and the 99th percentile quantile filtering were performed. Additionally, min–max normalization was applied to each marker to yield normalized data for further downstream analysis [39].

Unsupervised clustering and cell identification

To label each individual cell, we first employed the FlowSOM algorithm [40], resulting in the identification of 30 distinct clusters. Subsequently, we characterized each cluster as follows: for lymphocytes, B cells were identified as CD45 and CD20 double-positive cells, while $CD8^+$ T cells and $CD4^+$ T cells were distinguished by their high expression of CD45, CD3, and either CD8a or CD4. Regulatory T cells (Tregs) were differentiated based on their expression of Foxp3 and CD4. For myeloid cells, those exhibiting high levels of CD11c and HLA-DR were labeled as conventional dendritic cells (cDC), with CD66b marking neutrophils, CD14 indicating monocytes, and CD68 identifying macrophages. Among non-immune cells, those with elevated levels of CD31 were labeled as endothelial cells, while cells expressing high levels of fibroblast activation protein (FAP) or alpha-smooth muscle actin (αSMA) were distinguished as fibroblasts. Pan-keratin positive cells were classified as epithelial cells. Cells that expressed low levels of all markers were labeled as Unknown.

To further investigate the role of fibroblasts within the tumor microenvironment, we replicated the FlowSOM algorithm to identify the subclusters of fibroblasts. This analysis allowed us to distinguish various types of CAFs based on their marker expression levels, including Fibro_CD74, Fibro_GPNMB, Fibro_MYH11, Fibro_POSTN, and Fibro_TRPA1, alongside other CAFs. Additionally, we quantified the density of each cell type by counting the number of segmented cells of that type from each image.

Cellular neighbourhood identification

To identify spatial cellular neighborhoods (CNs), we first computed neighbor windows, defined as the N nearest cells surrounding each cell. Each neighbor window was represented as a frequency vector containing the distribution of cell types among the N nearest neighbors of the reference cell. These vectors were clustered to discover CNs. The analysis was performed for core tumor and peritumor regions using k-means clustering [41]. Finally, every cell was then assigned to a particular CN based on their neighbour window. These CNs can be spatially visualized and color-coded, while the cell phenotype fractions within each CN can also be quantified.

Fraction comparison

Fraction comparison was conducted to analyze differences in cellular subpopulations and CNs among patients stratified into distinct clinical groups. Specifically, the fractions of cellular subpopulations or CNs within various ROIs were calculated. For ROIs derived from the same patient, the fractions were averaged to reduce potential bias associated with ROI selection. To evaluate the significance of observed differences, a one-way analysis of variance (ANOVA) was applied.

Cell–cell pairwise interaction analysis

Pairwise cell–cell interaction analysis identifies cell phenotype pairs exhibiting either stronger co-localization ("interaction") or weaker co-localization ("avoidance") compared to a random distribution of cell phenotypes [39, 42]. Using a spatial cell graph previously constructed with Steinbock, the imcRtools package computes the average interaction count for each cell phenotype pair within a ROI [37]. This count is compared against an empirical null distribution generated by permuting all cell labels. For each cell phenotype pair within each ROI, an empirical P value is computed to assess statistical significance, where a value of 1 indicates interaction, 0 indicates no significance, and −1 indicates avoidance. These significance values could be aggregated across patients to determine pairwise cellular interactions at the cohort level.

Tumor patch detection and Fibro-Bar score computation

The Fibro-Bar Score was developed to quantify the spatial ratio of specific CAF and immune cell subpopulations at the tumor-stromal interface. The score is calculated based on key subpopulations prioritized by TiRank's spatial transcriptomic analysis and subsequently identified in the IMC data: three target CAF subpopulations (TRPA1 + CAF, MYH11 + CAF, and CD74 + CAF) and four target immune cell subpopulations (B cell, Plasma cell, CD8 + T cell, and CD4 + T cell).

The computation, visualized in Fig. 4F and adapted from Hoch et al. [43], follows a multi-step work for each ROI:

Tumor patch definition

Within pathologist-annotated core tumor regions, all epithelial tumor cells ($EpCAM^+$) are identified. A graph is constructed by connecting all two tumor cell pairs that are less than 20 μ m apart. Fully connected components within this graph that contain at least ten cells are designated as a 'tumor patch'.

Microenvironment hull expansion

A concave hull is constructed around the cells of each individual tumor patch. This hull is then expanded outward by a specified distance d to create a "patch microenvironment" that includes all cells (both tumor and non-tumor) within that distance of the patch boundary.

Fibro-Bar score calculation (per-patch)

For each patch, the score is calculated as the ratio of the summed fractions of the three target CAF subpopulations to the summed fractions of the four target immune cell subpopulations, considering only cells located within the expanded d-μm hull.

$$\text{Fibro-Bar Score}_{\text{patch}} = \frac{\sum \text{Frac}\,(\text{TRPA1+ CAF, MYH11+ CAF, CD74+ CAF})}{\sum \text{Frac}\,(\text{B cell, Plasma cell, CD8+ T, CD4+ T})}.$$

Patient-level score aggregation

This score is computed for all qualifying patches within an ROI. To mitigate potential sampling bias from ROI selection, the final Fibro-Bar Score for a given patient (used for correlation with TRG) is the average score taken across all ROIs analyzed for that patient.

This analysis was performed for multiple distances d = 1, 5, 10, 15, 20, 25, 30, 35, 40, 45, 50, and 100 μ m to assess the spatial stability of this relationship (Additional file 1: Fig. S21B). The $d = 20$ μm distance was used for the primary analysis (Fig. 4H) as it demonstrated a significant association with NACI non-responsiveness. The Fibro-Bar score provides a quantitative measure of immune exclusion by specific CAF subtypes within the tumor microenvironment.

Characterizing microenvironment dynamics of the Fibro-Bar

After computing the Fibro-Bar score, we investigated its association with protein expression of tumor cells, we applied Spearman correlation analysis to examine the relationship between the Fibro-Bar score and protein expression levels of tumor cells within a given tumor patch. To further investigate the dynamic of microenvironment of each cellular subpopulations, we compared protein expression differences among cellular subpopulations associated with tumor patches exhibiting either high or low Fibro-Bar scores. The analysis utilized fold change and Student's t-test to evaluate expression dynamics and statistical significance.

Identification of differential expression gene and enrichment pathways

Differentially expressed genes (DEGs) were identified using the FindMarkers function from the Seurat R package, applying the Wilcoxon rank-sum test. Genes were defined as differentially expressed if they met both of the following criteria: (1) a statistically significant difference in expression between the two groups, with a false discovery rate (FDR) below 0.05, and (2) an absolute log2-transformed fold change in expression greater than 0.5. Gene set enrichment analysis was implemented in the GSVA [44].

Pseudotime trajectory analysis

R package Monocle [45] was used to construct single-cell trajectories. We employed UMI counts and a negative binomial distribution to create the CellDataSet object. To identify differentially expressed genes before and after dabrafenib treatment, we used the FindMarkers function from R package Seurat. Dimensionality reduction was performed using the reduceDimension function with the DDRTree method. Finally, the orderCells function was applied for the ordering of cells in pseudotime.

Survival analysis

Survival analysis was performed using the R package survival. The surv_cutpoint function in R package survminer was utilized to determine the optimal cutting points for response-related signature enrichment scores. Kaplan–Meier (KM) survival curve was modeled by survfit function. Hazard ratio (HR) in univariate Cox regression were calculated by coxph function. The log-rank test was used to determine the statistical significance of differences between groups.

Statistics and reproducibility

Differentially expressed genes were identified using the Wilcoxon rank sum test, with false discovery rate correction using the Benjamini-Hochberg (BH) algorithm. The t-test was employed for comparisons between responders and non-responders. For multiple samples, ANOVA was used to compare the abundance deviation across three TRG groups. Boxplots were used to display the median, interquartile range (IQR), and 1.5 times the IQR (whiskers), with outliers exceeding 1.5 times the IQR included. For all statistical tests, a p-value or q-value less than 0.05 was considered statistically significant. All analyses were conducted using R (version 4.2.2) and Python (version 3.8.15).

Development of the GUI for TiRank

The GUI of TiRank was developed using the Python Dash framework (https://dash.plotly.com/), a Plotly product designed for creating and deploying data-driven applications with custom interfaces. TiRank-GUI is divided into six key sections: Homepage, Upload Data, Pre-processing, Analysis, Tutorial, and FAQs.

Results

Overview of TiRank

TiRank is an end-to-end toolbox designed to identify the clinically relevant cell subpopulations and spatial niches from scRNA-seq or ST data. Clinically relevant subpopulations and spatial niches refer to the organization of distinct cells within TME, which collectively influence clinical outcomes such as prognosis and therapeutic response [10, 46]. To achieve this, the TiRank workflow is structured into two distinct phases: a Training Phase that learns phenotype associations from bulk data, and an Inference Phase that applies the trained model to scRNA-seq or ST data (Additional file 1: Fig. S1). TiRank integrates three components, including the REO-transformation module, a multitask transfer learning framework and a Gaussian Mixture Model (GMM) based filter module, to facilitate the characterization of clinically relevant subpopulations and spatial niches (Fig. 1A). Specifically, for each clinical task, TiRank was trained exclusively on bulk transcriptomes with phenotype labels (Training Phase) and then applied to scRNA-seq or ST for inference (Inference Phase). Single-cell/spatial labels were reserved solely for evaluation (Additional file 1: Fig. S1).

The REO-transformation module serves as a preprocessing step for all data that utilizes gene pairs (GPs) to integrate multiple data modalities. GPs have been demonstrated to successfully prioritize candidate factors for conversion of cell fate and prognosis prediction [25, 26]. In TiRank, the REO-transformation module converts expression profiles of bulk, single-cell and spatial transcriptomics into phenotypic gene pair (PGP) matrices, respectively. PGP matrices represent the relative expression levels of phenotype-associated genes (Additional file 1: Fig. S1A). This transformation not only mitigates biases across transcriptomic modalities but also ensures that phenotypic information is effectively embedded in the data. By simplifying the complexity of the high-dimensional expression profile, the output of the REO-transformation module makes it easier for the multitask learning framework to generate more robust low-dimensional representations.

Following this, the multitask transfer learning framework builds on the features generated by the REO-transformation module. It consists of an encoder, projection heads and loss functions. They were designed to learn low-dimensional representations from multimodal data. During the training phase, these representations preserve both phenotypic information (learned from the bulk data), as well as cellular and spatial relationships (learned unsupervised from scRNA-seq/ST data; Additional file 1: Fig. S1B and C), allowing for the accurate prediction of TiRank scores (Additional file 1: Fig. S1D). These scores quantify the degree of association between individual cells or spots and the phenotype of interest. By leveraging the PGP matrices created by the REO module, the multitask learning framework can effectively integrate multimodal data, yielding informative representation and facilitating the identification of clinically relevant subpopulations and spatial niches.

After obtaining the TiRank scores from the inference phase, we observe that the score distribution follows a mixture of Gaussian distributions. Based on this observation, we apply a GMM to decompose the distribution and classify individual cells or spots into three categories: TiRank$^+$, TiRank$^-$ and phenotype-independent. This GMM is first fit on the scores from the bulk training data to establish objective boundaries, which are then applied to the new scRNA-seq/ST scores. TiRank$^+$ refers to cells or spots that are positively correlated with the target phenotype, such as poor prognosis, early relapse, or resistance to therapy. TiRank$^-$ indicates cells or spots that are negatively correlated with the phenotype, such as favorable prognosis, non-relapse, or sensitive to therapy. The phenotype-independent category includes cells or spots with weak or no correlation to the target phenotype, representing biological 'bystanders' not actively driving the clinical outcome. This three-category classification is chosen based on the hypothesis that only a subset of cells or spots will exhibit a clear positive or negative correlation with the target phenotype, while the remaining show weak or no association, necessitating a third neutral category. The GMM-based filtering of these ambiguous cells ensures downstream analyses focus on high-confidence signals, particularly valuable in noisy clinical data. Subsequently, TiRank assigns each cell or spot to one of these categories (Fig. 1A).

TiRank performs drug response prediction of cell subpopulations

We evaluated the drug response prediction performance of TiRank using public datasets, including five scRNA-seq and eight bulk transcriptomics datasets from cell lines treated with four drugs: Cisplatin, Docetaxel, Erlotinib, and Gefitinib (Methods). These datasets included binary drug response labels for individual cells [47] (Additional file 2: Table S1). To assess the performance of TiRank, we compared it to three state-of-the-art algorithms: Scissor [17], DEGAS [18] and Beyondcell [32]. Models were trained exclusively on bulk and then applied to scRNA-seq for inference; single-cell labels were used only for evaluation. TiRank demonstrated superior performance in terms of F1-score, accuracy, and recall (Fig. 1B-D), with scores ranging from 0.7 to 0.9 across the evaluated datasets. These metrics measured the ability of the algorithm to both correctly identify positive drug responders and minimize false positives. Furthermore, time-efficiency experiments emphasized the scalability of TiRank, with runtime varying from several seconds to a

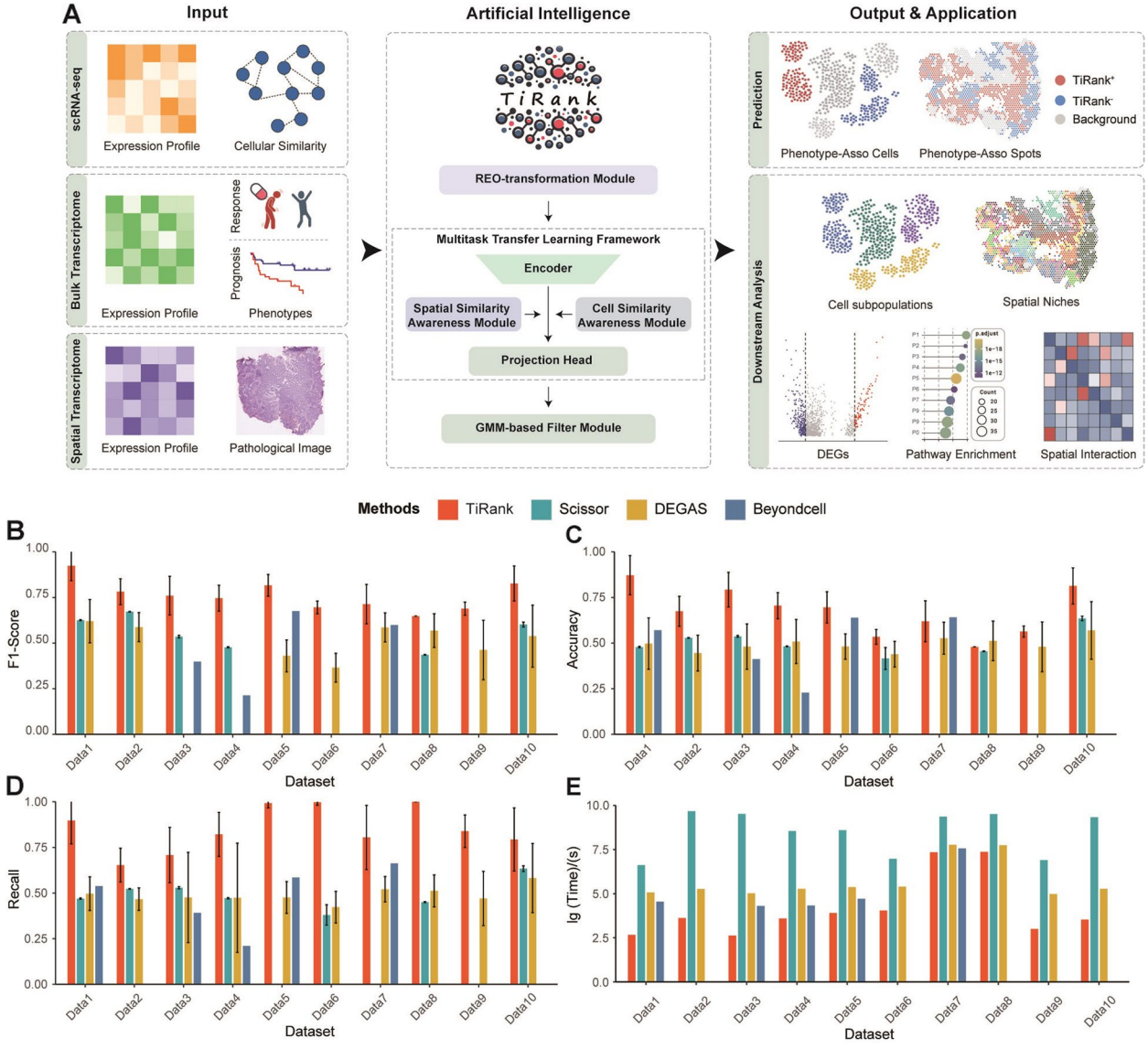

Fig. 1 TiRank overview and performance on drug response datasets. **A** Schematic overview of the TiRank framework. The workflow consists of three components: input, computational modules, and output with downstream applications. Inputs include bulk transcriptomics with clinical phenotypes (e.g., prognosis or treatment response), scRNA-seq, or ST data. TiRank incorporates a REO-transformation module, a multitask transfer learning framework, and a Gaussian mixture model-based filter. The multitask transfer learning framework includes an encoder and prediction head, along with Cell Similarity Awareness Module and the Spatial Similarity Awareness Module, to learn low-dimensional representations for integrating individual cells or spots with clinical information. The Gaussian mixture model-based filter retains cells or spots strongly associated with phenotypes and enhances prediction accuracy. Outputs include phenotype-associated cells or spatial spots, enabling the identification of clinically relevant cellular subpopulations and spatial niches. TiRank^{+} refers to cells or spots associated with poor prognosis, early relapse, or resistance to therapy. TiRank^{-} indicates cells or spots associated with favorable prognosis, non-relapse, or response to therapy. The background represents phenotype-independent cells or spots. **B**-**D** Performance comparison of TiRank, Scissor, DEGAS, and Beyondcell in predicting drug response across 10 datasets. For each dataset contains specific drug, model was trained only on bulk (GDSC/CCLE), then applied to scRNA-seq for inference, and single-cell drug labels were used exclusively for evaluation. Bar plots show (**B**) F1-scores, (**C**) accuracy, and (**D**) recall for each method, with TiRank (orange), Scissor (teal), DEGAS (yellow), and Beyondcell (blue). Cell scores are mapped to labels using the bulk-fitted three-component GMM (default T = 0.05) and neutral cells are not included in binary metrics. Missing bars (marked N/A in the figure) indicate datasets where a method failed to produce results due to specific tool limitations. Beyondcell requires pre-defined drug sensitivity signatures that were not available for all datasets, and Scissor imposes strict data correlation requirements that were not met in all cases. Each method was evaluated 50 times per dataset, with error bars representing standard deviations. **E** Computational efficiency of the methods. Bar plot displays the log-transformed execution time (in seconds) for each method across the 10 datasets, highlighting the efficiency of TiRank relative to Scissor, DEGAS, and Beyondcell

few minutes depending on the dataset size, underscoring its potential for large-scale data analysis (Fig. 1E).

To further understand the performance of TiRank, we conducted three experiments evaluating its key components. First, using GPs as input features improved TiRank's F1-score by 5% to 10% compared to individual genes (Additional file 1: Fig. S2A). Second, we compared encoder models, including multilayer perceptron (MLP), DenseNet [48], and Transformer [49]. Although Transformer yielded the highest performance, MLP offered comparable results with greater computational efficiency (Additional file 1: Fig. S2B). This indicates that GPs effectively capture phenotype information, reducing dependence on encoder complexity. Third, an ablation study showed that the bulk loss term was essential for accurate phenotype prediction, while the regularization loss, though less critical for performance, preserved biological connectivity among cellular subpopulations (Additional file 1: Fig. S2C). Finally, to provide statistical justification for our GMM-based filter, we performed a comparative analysis. This analysis confirmed that our GMM approach is better than other models like 1D k-means and manual cutoff, and is robust to its threshold parameter (Additional file 1: Fig. S3A).

Applying TiRank to a specific dataset, we demonstrated its ability to track evolutionary dynamics in drug-treated cells. In an scRNA-seq dataset from Dabrafenib-treated SKMEL28 melanoma cells, TiRank predicted increasing drug-resistance scores over three days (Additional file 1: Fig. S3B-D), reflecting cellular evolutionary dynamics under drug pressure. Pseudotime analysis further revealed rising resistance scores along the trajectory from day 0 to day 3 (Additional file 1: Fig. S3E, F), validating the ability of TiRank to prioritize therapeutic phenotypes and elucidate treatment-induced evolutionary trends.

Finally, to investigate the translational potential of TiRank, we performed an additional benchmark to assess if a model trained only on bulk cell line data could predict patient response in clinical scRNA-seq cohorts. Using the datasets provided from Sinha et al. [50], we trained TiRank on DepMap bulk data to predict response in two patient scRNA-seq cohorts: breast cancer (BRCA) and non-small cell lung cancer (NSCLC). TiRank significantly outperformed other methods, achieving an Area Under the Curve (AUC) of 0.738 in BRCA and 0.887 in NSCLC, demonstrating a robust ability to translate cell line-derived insights to clinical data (Additional file 1: Fig. S3G-H; Additional file 1: Supplementary Methods).

Overall, these results demonstrate the feasibility of TiRank to prioritize individual cells with therapeutic phenotypes from scRNA-seq data through the established multitask transfer learning framework.

TiRank infers cellular subpopulations with clinical significance in human cancers

To assess the ability of TiRank in identifying clinically significant cellular subpopulations, we analyzed six scRNA-seq datasets and 25 bulk transcriptomics datasets, with survival information, from lung adenocarcinoma (LUAD), hepatocellular carcinoma (HCC), GC, colorectal cancer (CRC) and acute myelogenous leukemia (AML) [51] (Additional file 2: Table S1). TiRank was then applied to these datasets by integrating gene expression and survival information, identifying prognostic cell subpopulations across these cancers (Fig. 2A).

We compared performance of TiRank against two established algorithms, Scissor and CIBERSORT [52], across five cancer types (Additional file 2: Table S1). For this evaluation, we first established a ground truth by conducting a systematic literature review, conclusion collection, and downstream evidence evaluation to define favorable or poor prognostic associations for cell subpopulations (Additional file 1: Fig. S4 and Additional file 2: Table S2). Cell subpopulation annotations, derived from the original datasets [53–57] (Additional file 1: Fig. S5), were then used to apply this ground truth to the scRNA-seq data. TiRank demonstrated high precision (0.69 to 1.00) and low false rates in identifying prognosis-associated subpopulations across all cancer types, outperforming Scissor (precision: 0.24 to 0.44) and CIBERSORT (precision: 0.50 to 1.00, with some datasets yielding NA). Furthermore, TiRank exhibited robust coverage, accurately predicting prognostic outcomes across diverse bulk transcriptomics datasets, which underscores its potential for clinical applications (Fig. 2B and Additional file 1: Fig. S6).

Building on its success in identifying prognostic cell subpopulations, we further applied TiRank to identify cell populations associated with the efficacy of immune checkpoint blockade (ICB) therapy in melanoma. Using one scRNA-seq dataset [58] and four independent bulk transcriptomics datasets [59–62], TiRank identified 174 TiRank^{+} cells (associated with ICB resistance, primarily in clusters 7 and 18) and 722 TiRank^{-} cells (associated with ICB response, predominantly in clusters 10 and 17) from a total of 5,928 cells divided into 20 clusters (Additional file 1: Fig. S7A-C). Differential expression analysis revealed that *SLC11A1*, *VCAN*, and *S100A9* were highly expressed in TiRank^{+} cells, while *HMGB1*, *IL2RG*, and *IL32* were upregulated in TiRank^{-} cells (Additional file 1: Fig. S7D, 8 A). These findings indicate that TAMs contribute to ICB resistance, whereas B and T cells are linked to ICB response (Additional file 1: Fig. S8B, C) [62, 63]. Pathway enrichment analysis highlighted elevated TNFα signaling and PD-1 expression, aligning with prior

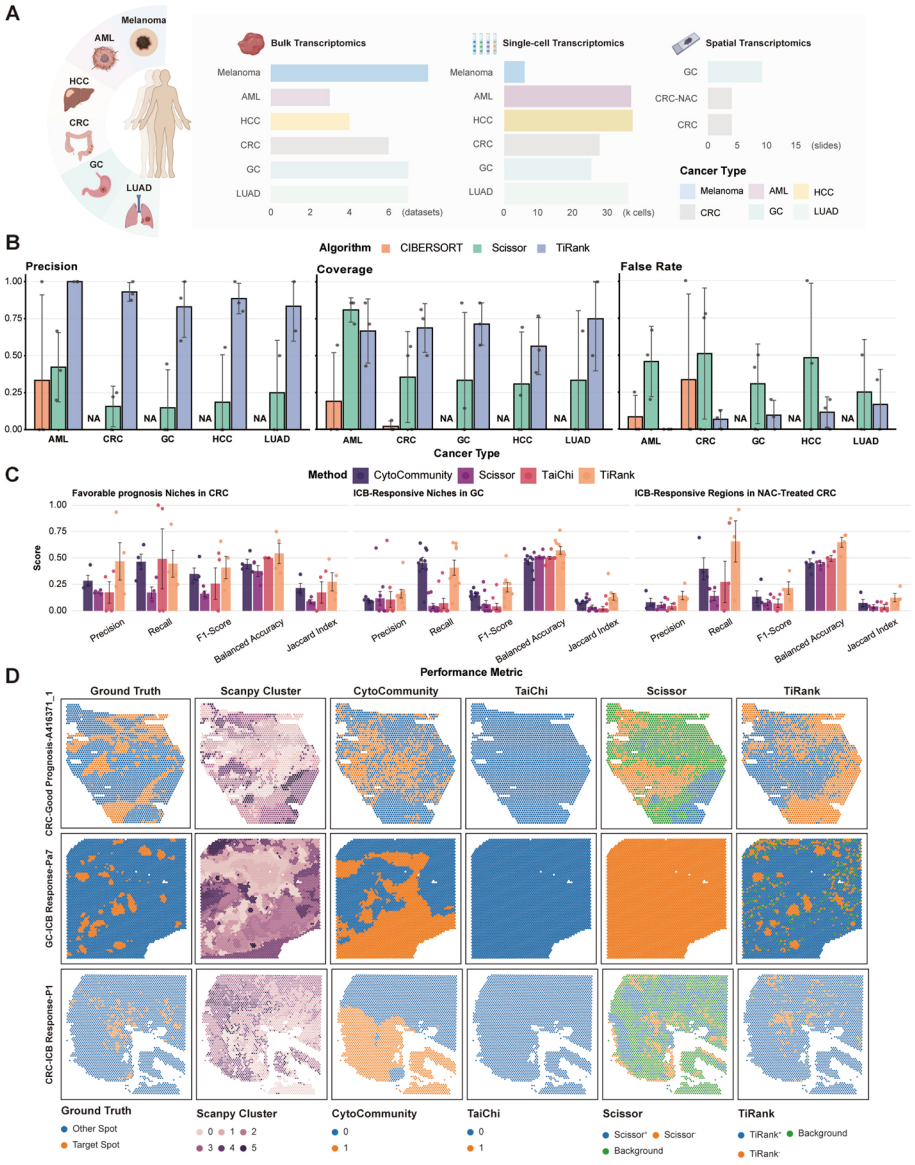

Fig. 2 TiRank identifies clinically relevant cellular subpopulations and spatial niches across human cancers. **A** Overview of transcriptomes used to evaluate the performance of TiRank on clinical cohorts. A total of 25 bulk transcriptomic datasets and 6 single-cell RNA sequencing (scRNA-seq) datasets, spanning melanoma, AML (acute myeloid leukemia), HCC (hepatocellular carcinoma), CRC (colorectal cancer), GC (gastric cancer), and LUAD (lung adenocarcinoma), were analyzed to identify clinically significant cellular subpopulations. Additionally, 19 bulk transcriptomic datasets and 27 spatial transcriptomic (ST) slides were used to uncover spatially organized phenotypic niches and interactions. **B** Performance comparison of TiRank, Scissor, and CIBERSORT in predicting prognosis-associated cellular subpopulations across five cancer types (AML, CRC, GC, HCC, LUAD). Bar plots display precision, coverage, and false rate for each method, with TiRank (orange), Scissor (teal), and CIBERSORT (purple). Precision represents the proportion of correctly predicted associations among all positive predictions. Coverage measures the algorithm's ability to identify phenotype-associated subpopulations across bulk and scRNA-seq data pairs. False rate indicates the proportion of incorrect positive predictions among all positive predictions. For each phenotype/cancer pair, model was trained only on bulk transcriptomics data, then applied to scRNA-seq for inference; predicted subpopulations were evaluated against literature-curated ground truths. **C** Performance comparison of TiRank, Scissor, CytoCommunity, and TaiChi in predicting phenotype-associated spatial niches across three clinical settings: favorable prognosis niches in CRC, immune checkpoint blockade (ICB)-responsive niches in GC, and ICB-responsive regions in neoadjuvant chemotherapy-treated CRC. Bar plots show precision, recall, F1-score, balanced accuracy, and Jaccard index for each method, with CytoCommunity (purple), Scissor (pink), TaiChi (orange), and TiRank (blue). Error bars represent the standard deviation of predictions across slides within each dataset. **D** Representative examples of phenotypic niche predictions from panel C. Each row corresponds to an individual slide, and each column represents a method or ground truth. Ground truth, determined by manual annotations, labels target spots (orange) associated with the phenotype and other spots (blue) as background. Scanpy clustering shows gene expression-based clusters (0–5). Predictions by CytoCommunity, TaiChi, Scissor, and TiRank highlight spots predicted as phenotype-associated (orange) versus background (blue)

evidence that the exhausted state of CD8⁺ T cells can be reinvigorated by ICB therapy [64] (Additional file 1: Fig. S8C, D). Lastly, an ICB-response gene signature derived from upregulated genes in TiRank⁻ cells correlated with higher ICB response rates and longer survival in four bulk transcriptomics datasets (Additional file 1: Fig. S7E). Collectively, these findings underscore the ability of TiRank to identify ICB-responsive cell subpopulations in melanoma and highlight its broader potential for elucidating therapeutic targets in cancers.

TiRank prioritizes clinically relevant spatial niches in cancer

We then applied TiRank to integrate bulk transcriptomics and ST data, identifying spatial niches linked to clinical outcomes across two cancer types (Fig. 2A, Additional file 2: Table S1). To assess its performance, we benchmarked TiRank against three algorithms, including Scissor, CytoCommunity [65], and TaiChi [66]. These methods were not originally designed for patient-label-free ST data analysis, despite their potential relevance (Additional file 2: Table S7).

Three clinical datasets were evaluated, each addressing distinct clinical questions (Methods). First, in four treatment-naïve CRC ST slides from Valdeolivas et al. [67], CMS1-type CRC with high immune cell infiltration correlated with favorable prognosis. TiRank, combined with prognosis bulk transcriptomics data, identified niches of high immune infiltration. Second, in four ST slides from CRC patients treated with neoadjuvant chemotherapy, Wu et al. [68] associated high CD8⁺ T cell infiltration with ICB response. Using bulk transcriptomics with ICB efficacy data, TiRank pinpointed regions with elevated CD8⁺ T cell presence. Third, in a retrospective cohort of nine treatment-naïve GC patients, prior studies [37, 69] linked tertiary lymphoid structures (TLS) to ICB response. TiRank, integrating ICB response bulk transcriptomics data, inferred TLS presence in ST slides of GC. Across these scenarios, TiRank outperformed other algorithms on five metrics, including Precision, Recall, F1-score, Balanced Accuracy, and Jaccard Index, which measured agreement with human-annotated ground truth (Fig. 2C). Specifically, TiRank distinguished target regions, such as high immune infiltration zones in CRC and TLS in GC, from background areas, while Scissor and TaiChi showed inconsistent performance across slides (Fig. 2D, Additional file 1: Fig. S9 and 10).

To further illustrate the potential of TiRank in discovering clinical biomarkers, we analyzed a bulk transcriptomics dataset with overall survival (OS) and ten ST slices from CRC patients [67]. Combined with pathological region annotations, TiRank revealed that immune cell-enriched regions (IC_Aggre) were associated with favorable prognosis, while fibroblastic regions (Stroma Fibroblastic) were correlated with poor prognosis (Additional file 1: Fig. S11A and B). Fibroblastic regions are known to play critical roles in shaping the TME and influencing CRC patient outcomes [70, 71]. Focusing on these fibroblastic areas, we decomposed the cellular composition of individual spots using well-annotated scRNA-seq data (Additional file 1: Fig. S12A) [35]. TiRank⁺ spots (linked to poor prognosis) were enriched with myofibroblasts, mast cells, and SPP1⁺ TAMs, whereas TiRank⁻ spots (associated with favorable prognosis) were characterized by NK cells, smooth muscle cells (SMCs), and intermediate cells (Additional file 1: Fig. S11C and Additional file 1: Fig. S12C). Spatial analysis [35, 36] revealed significant co-localization of SPP1⁺ TAMs and myofibroblasts within TiRank⁺ spots (Additional file 1: Fig. S11D, Additional file 1: Fig. S12D and Additional file 1: Fig. S13). Differential gene expression and pathway enrichment analysis further indicated that TiRank⁺ spots were associated with activation of the IL-17 and TNF pathways (Additional file 1: Fig. S11E, Additional file 1: Fig. S12B), both of which play critical roles in stress response and promote tumor progression in CRC [72, 73]. To confirm this prognostic association, we derived a TiRank⁺ spot signature (144 DEGs; Additional file 1: Fig. S12B) and scored four independent CRC cohorts by ssGSEA. Kaplan–Meier analyses showed that patients with high TiRank⁺ signature scores had significantly worse survival (Additional file 1: Fig. S12E), validating the clinical relevance of the poor-prognosis niches identified by TiRank. In summary, TiRank highlights the spatial co-localization of myofibroblasts and SPP1⁺ TAMs in shaping the TME and their association with poor prognosis in CRC [74, 75]. These findings further demonstrate that TiRank is a powerful tool for uncovering spatial niches associated with prognosis and drug response in clinical cohorts.

TiRank dissects therapeutic responsive niches in gastric cancer

Previous experiments on pan-cancerous ST data underscore the potential of TiRank in uncovering critical spatial niches and facilitating the discovery of clinical biomarkers. Here, we applied TiRank to identify spatial niches associated with treatment efficacy in GC. Three bulk transcriptomics datasets from independent clinical cohorts with different treatment strategies were included: GSE66229 [76] with adjuvant chemotherapy (AC); Kim2018 and Kwon2021 [77, 78] with ICB treatment (Additional file 2: Table S1); and UnionH Cohort 1 (UnionH-1) with NACI therapy from our retrospective UnionH dataset. Additionally, we collected UnionH Cohort 2 (UnionH-2) including surgical samples from nine treatment-naïve patients with spatial transcriptomes (Fig. 3A and Additional file 2: Table S3).

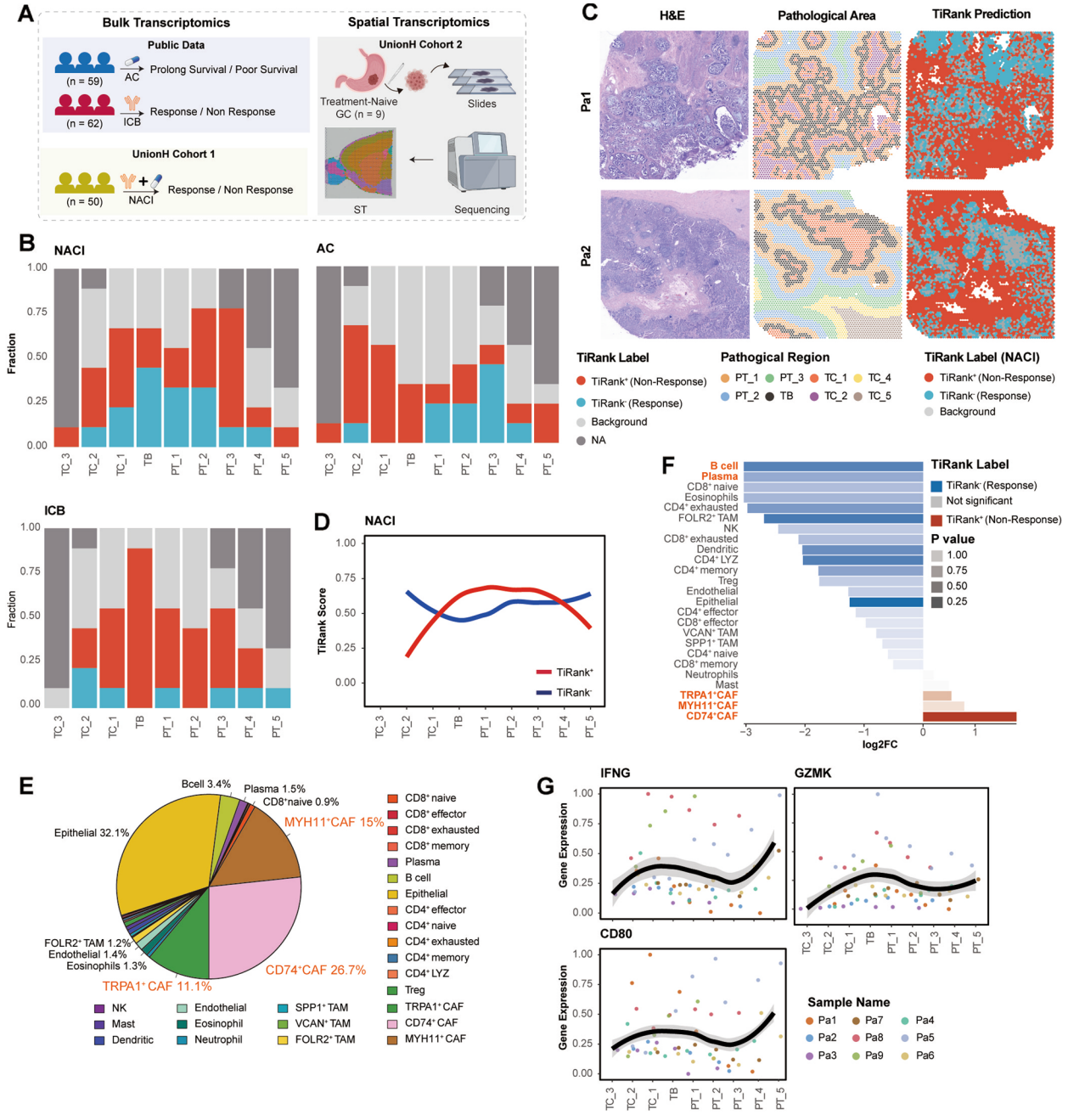

Fig. 3 Characterizing spatial tumor heterogeneity associated with NACI in GC. **A** Bulk transcriptomes and spatial transcriptomes of GC used in this study. Two public bulk transcriptomics datasets included GC patients treated with adjuvant chemotherapy (AC) or ICB alone. Two in-house datasets: UnionH-1, a retrospective cohort, involved GC patients receiving NACI with bulk transcriptomics sequencing, while UnionH-2 comprised nine GC patients without pre-surgery treatment, analyzed using ST. TiRank was applied to identify spatial niches associated with distinct treatment responses in ST slides. **B** Stacked bar plots showing TiRank-predicted treatment resistance (TiRank^{+}, red) or responsiveness (TiRank^{-}, blue) across distinct spatial regions of GC tissues, with gray representing unclassified regions. The x-axis represents spatial regions (PT, peritumor; TC, tumor core; TB, tumor boundary), and the y-axis displays the proportion of classifications across nine GC samples. **C** Spatial mapping of TiRank predictions in two representative tissue slices. Left: H&E-stained images. Middle: Pathological regions annotated using the Cottrazm package. Right: TiRank classifications for NACI response, with red indicating treatment resistance (TiRank^{+}), blue denoting responsiveness (TiRank^{-}), and gray representing background. Additional file 1: Fig. S14 shows additional tissue slices and predictions for other therapies. **D** Spatial distribution of TiRank scores in GC tissues. TiRank^{+} (red) spots represent regions predicted to be associated with NACI resistance, while TiRank^{-} (blue) indicates predicted responsiveness. Scores were averaged across spatial regions for all nine treatment-naive samples. **E** Cellular composition of the tumor boundary, deconvoluted using CARD. Top 10 cell types are shown. **F** Differential cell fraction analysis between TiRank^{+} (resistant) and TiRank^{-} (responsive) spots within the tumor boundary. X-axis shows fold change. CAFs are associated with resistance (TiRank^{+}), while immune cells are associated with response TiRank^{-}. **G** Gene expression dynamic across spatial regions. The average expression levels of IFNγ, GZMK and CD80 across spatial regions from the core tumor to the peritumor area. Each point represent the average gene expression at each point for individual patients. Curve represents the mean values ± standard deviation

Each ST slide was segmented into distinct spatial regions, including tumor core, tumor boundary, and peritumor regions using Cottrazm [34] (Additional file 1: Fig. S14). TiRank was then used to integrate bulk transcriptomes with individual ST slices, linking each spatial spot to the responsiveness of specific treatment regimens. The results showed that the tumor boundary niche correlated with resistance to AC or ICB alone but exhibited responsiveness to combined chemoimmunotherapy (Fig. 3B, C, and Additional file 1: Fig. S14). Moreover, the TiRank labels within the tumor boundary exhibited substantial heterogeneity (Fig. 3D), with the spatial distribution of TiRank scores significantly increasing in the tumor boundary region (Additional file 1: Fig. S15A). These findings underscore the potential importance of the tumor boundary microenvironment in shaping the response to combined chemoimmunotherapy.

We further decomposed the cellular composition of spots in the tumor boundary niche [79] (Additional file 1: Fig. S15B). The results revealed a predominance of tumor cells, CAFs, endothelial cells, plasma cells and B cells (Fig. 3E and Additional file 1: Fig. S15C). Differential cell subpopulation fraction analysis indicated that CAF subpopulations were enriched in spots associated with combined chemoimmunotherapy resistance, while immune cells were enriched in spots linked to response within the tumor boundary niche (Fig. 3F and Additional file 1: Fig. S16). Collectively, these findings highlight the spatial arrangement of CAFs and immune cells as highly correlated with combined chemoimmunotherapy efficacy within the tumor boundary, suggesting its potential value in guiding precision treatment in GC.

To better understand the molecular mechanisms underlying the tumor boundary niche, we analyzed gene expression changes relative to the distance from the tumor boundary. Cytotoxic and immune-activating molecules, such as INFG, GZMK, and CD80, were upregulated from the tumor core to the boundary region (Fig. 3G). Pathway enrichment analysis further revealed that combined chemoimmunotherapy-resistant spots within the boundary region were associated with IL-17 and B cell receptor signaling pathways, Wnt and purine metabolism pathways (Additional file 1: Fig. S15D). These observations suggest that the spatial distribution and transcriptional dynamics within the tumor boundary are associated with tumor progression, immune exclusion, and ICB resistance in GC and other cancers [80–83].

In summary, TiRank elucidates the associations between spatial niches and treatment regimens in GC, emphasizing the potential value of the tumor boundary niche in predicting treatment efficacy. Several cell subpopulations, including CD74$^+$ CAFs, TRPA1$^+$ CAFs, MYH11$^+$ CAFs, B cells, plasma cells and T cells, were concentrated in the tumor boundary niche and exhibited inverse correlations with combined chemoimmunotherapy efficacy. These findings enhance our understanding of the molecular mechanisms influencing therapy outcomes and contribute to the development of novel indicators for selecting GC patients who may benefit from combined chemoimmunotherapy.

IMC validates spatial organization of CAFs and immune cells

Previous analyses utilizing TiRank on bulk and spatial transcriptomics highlighted the importance of the tumor boundary niche, particularly the diverse CAF and immune subpopulations, in guiding GC patients toward NACI response (Fig. 4A). To further validate the spatial distribution of CAFs and immune cells within the TME that associate with NACI response, IMC was performed on pre-treatment gastroscopy samples from ten GC patients (Additional file 1: Fig. S17A and Additional file 2: Table S4). Our custom-designed IMC panel targeted 35 proteins, including markers for immune and non-immune cells, as well as proteins related to immune status and metabolism, enabling a comprehensive analysis of cellular compositions (Fig. 4B, C and Additional file 1: Fig. S17B). Cell segmentation and protein quantification via Steinbock [37] identified a total of 498,593 cells from 61 images. Subsequent unsupervised cell clustering algorithm identified ten distinct cell types and 26 subpopulations, including five CAF subtypes and six TAM subtypes (Fig. 4D, E and Additional file 1: Fig. S18A-C). Abundance comparisons and spatial analysis were performed to reveal features associated with different TRG. B cells, plasma cells and conventional dendritic cells (cDCs) were significantly enriched in patients with TRG 0, who demonstrated a complete response to NACI (Additional file 1: Fig. S18D). For CAF subpopulations, no significant frequency differences between TRG groups were observed (Additional file 1: Fig. S18E). As for subpopulations of TAM, CD74$^+$ macrophages were enriched in images associated with NACI responders, while CD80$^+$ macrophages showed the opposite pattern (Additional file 1: Fig. S18F), in line with previous research [69].

Furthermore, we performed cellular neighborhood (CN) analysis by integrating the spatial neighbors of individual cells [84]. This approach identified eight distinct CN types, revealing diverse cellular niches within the core tumor of GC samples. These niches were characterized by varying abundances of cell populations, including epithelial cells, macrophages, T cells, B cells, neutrophils, fibroblasts, and endothelial cells (Additional file 1: Fig. S19A). Spatial distribution maps further illustrated the heterogeneity of these CN types across different regions of interest, highlighting dynamic interactions between immune cells and other components of the TME (Additional file 1: Fig. S19C). However, statistical analysis revealed that these CN types did not exhibit a

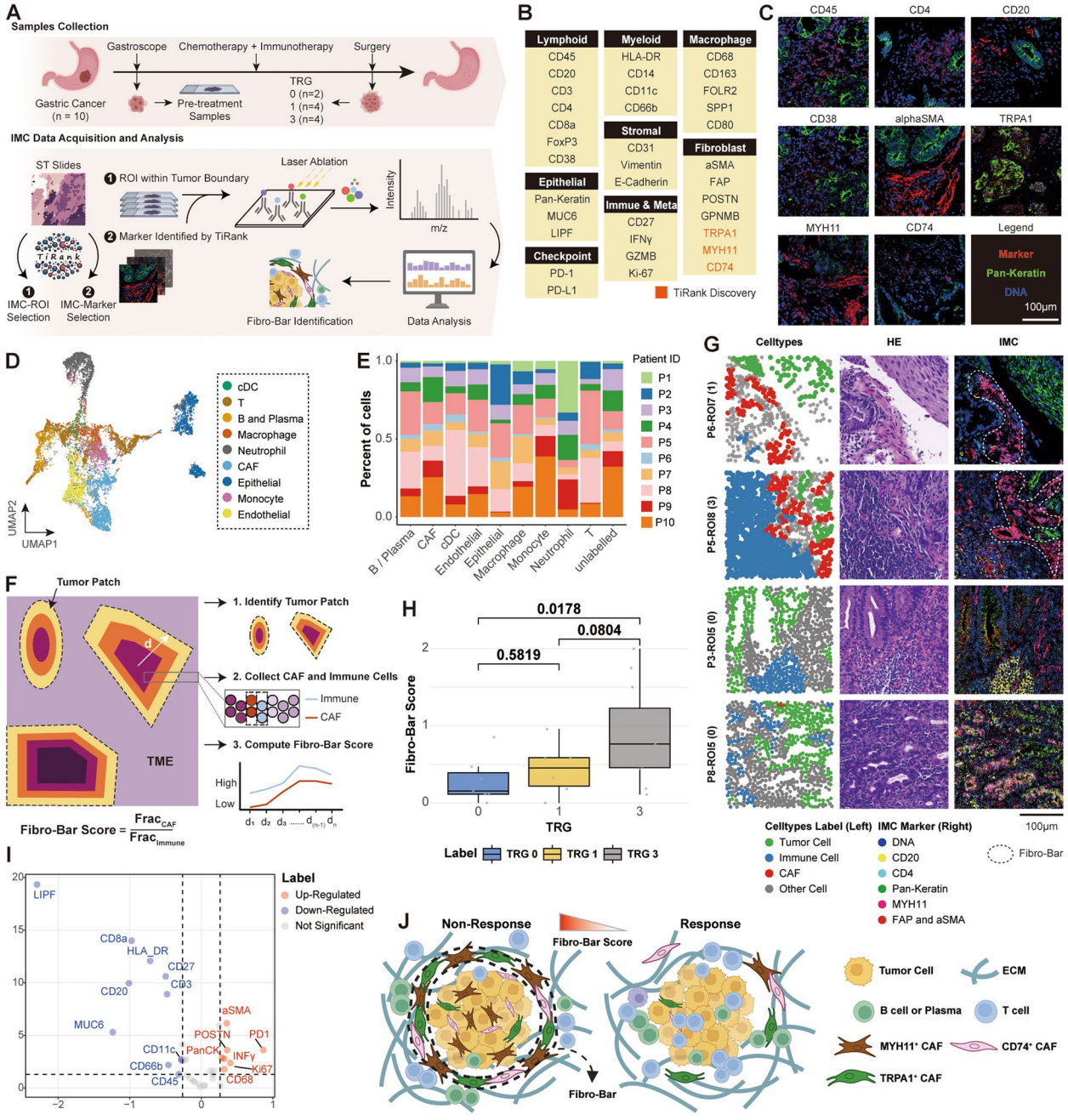

Fig. 4 (See legend on next page.)

(See figure on previous page.)

Fig. 4 Validation of Fibro-Bar in spatial proteomics of GC receiving NACI. **A** Schematic overview of the downstream validation of Fibro-Bar, identified by TiRank in spatial transcriptomics (ST), using Imaging Mass Cytometry (IMC). Union-H3 cohort included pre-treatment gastroscopic samples from 10 GC patients undergoing NACI, which were analyzed to assess treatment response via tumor regression grade (TRG 0–3). Regions of interest (ROIs) and markers were selected based on ST data analyzed by TiRank, focusing on tumor boundary regions and the spatial distribution of cancer-associated fibroblasts (CAFs) and immune cells. The IMC workflow included laser ablation, data collection, and downstream analysis to evaluate Fibro-Bar's association with NACI efficacy. **B** Antibody panel of 35 protein markers used to identify and classify distinct cell subpopulations, including lymphoid (e.g., CD3, CD4), myeloid (e.g., CD68, CD163), epithelial (e.g., Pan-Keratin), fibroblast (e.g., FAP, αSMA), and metabolic (e.g., MYH11) markers, alongside TiRank-discovered targets. **C** Representative IMC images showing the expression of key markers in CAFs and immune cells. Tumor cells are labeled with Pan-Keratin (green), nuclei with Iridium (blue), and specific markers (e.g., CD45, CD4, CD20, FAP, αSMA, MYH11) with red. Scale bar, 100 μm. **D** UMAP visualization of major cell types across samples, including T cells, B cells, dendritic cells (DCs), macrophages, CAFs, monocytes, epithelial cells, and endothelial cells. Unlabeled cells were excluded from the analysis. **E** Stacked bar plot showing the relative proportions of cell types across 10 patient samples (P1–P10). **F** Workflow for calculating the Fibro-Bar score, which quantifies the spatial positioning of CAFs and immune cells at the tumor patch border. The process involves: (1) identifying tumor patches, (2) collecting CAF and immune cell and calculating fractions, and (3) computing the Fibro-Bar score based on CAF and immune cell fractions at the tumor boundary (d = 20 μm). **G** Zoomed-in IMC images illustrating Fibro-Bar niches across ROIs with distinct TRG labels. P6-ROI7 and P5-ROI8 represent high Fibro-Bar scores, characterized by elevated CAF infiltration relative to immune cells at the tumor boundary, associated with higher TRG. P3-ROI5 and P8-ROI5 show lower Fibro-Bar scores, with immune cell infiltration and lower TRG. Left column: Cell-type composition (tumor cells, CAFs, immune cells). Middle column: Hematoxylin and Eosin (H&E) staining. Right column: IMC images highlighting DNA (blue), MYH11 (pink), Pan-Keratin (green), CD20 (yellow), CD4 (cyan), FAP, and αSMA (red). White arrows indicate Fibro-Bar niches. Scale bar, 100 μm. **H** Boxplots comparing Fibro-Bar scores across TRG categories (TRG 0–3). Statistical significance assessed using a two-sided Student's t-test. **I** Volcano plot of differentially expressed markers between high and low Fibro-Bar score tumor patches (d = 20 μm). All cells within tumor patch were involved in computation. Red dots indicate proteins upregulated in high Fibro-Bar score patches, and blue dots indicate proteins upregulated in low Fibro-Bar score patches. **J** Schematic representation of Fibro-Bar in the TME. Tumor patches with high Fibro-Bar scores, marked by CAF-coated tumor cells and immune cell exclusion, are associated with reduced responses to NACI in GC, while low Fibro-Bar scores correlate with increased immune cell infiltration and better responses

significant association with TRG in GC patients treated with NACI (Additional file 1: Fig. S19B and C). These findings emphasize the need for a more tailored analytical approach and specific biomarkers to effectively stratify GC patients who may benefit from NACI.

Fibro-Bar score predicts NACI response in GC

IMC analysis revealed that the abundance of CAF subpopulations and CN types did not significantly differ across TRG stages. However, IMC enabled detailed examination of their spatial distribution at the interface between tumor cells and TME components within tumor patches. Here, we first defined tumor patches as aggregates of tumor cells and extended this hull to include neighboring TME components [43] Specific CAF subpopulations ($TRPA1^+$, $MYH11^+$, $CD74^+$) and immune cells (B cells, plasma cells, $CD8^+$ T cells, $CD4^+$ T cells), previously identified by TiRank (Fig. 3F), showed distinct spatial distribution at this boundary (Fig. 4G). This region, termed the "Fibro-Bar" niche, exhibited a barrier-like aggregation of CAFs that excluded immune cells (Additional file 1: Fig. S20).

The "Fibro-Bar Score", defined as the ratio of CAF to immune cell fractions within tumor patches (Fig. 4F), was developed to quantify this spatial arrangement. Computed across various distances (d) from tumor patches, the score demonstrated a significant association with non-responsiveness to NACI at d equal to 20 μm, with consistent trends at greater distances (Additional file 1: Fig. S21B). This metric effectively distinguished GC patients likely to benefit from NACI, and it was better than the single abundance of CAFs or T cells (Fig. 4H and Additional file 1: Fig. S21A).

Protein expression analysis further elucidated the Fibro-Bar niche's role. CAF-associated proteins (e.g., αSMA, POSTN) positively correlated with higher Fibro-Bar scores, while immune-associated markers (e.g., HLA-DR, CD8a) showed negative correlations (Additional file 1: Fig. S21C). In high-Fibro-Bar score tumor patches, differential expression analysis revealed that upregulation of αSMA, POSTN, and Ki67, alongside downregulation of HLA-DR, CD8a, and CD20, indicating a CAF-enriched boundary that impedes immune cell infiltration (Fig. 4I). Focusing on B and T cells, significant upregulation of PD-1 and IFNγ, markers linked to immune checkpoint blockade response [85, 86] (Additional file 1: Fig. S21D). It suggested that elevated CAF presence may impair immune cell functionality in tumor elimination [82].

The Fibro-Bar Score outperformed the barrier score proposed by Enfield et al. [87] in identifying GC patients responsive to NACI (Additional file 1: Fig. S21E), highlighting distinct spatial rearrangements of CAFs and immune cells within the tumor niche (Fig. 4J). This discovery also underscores the value of TiRank as a comprehensive computational platform for systematic prioritization of clinically relevant niches for precision oncology.

Graphical user interface for TiRank

We developed a user-friendly graphical user interface (GUI) for TiRank to enhance accessibility for researchers and clinicians (Fig. 5A). The GUI enables users to upload gene expression profiles from bulk transcriptomics, scRNA-seq, and ST, along with corresponding clinical phenotypes from bulk transcriptomics. Subsequently, TiRank performs data preprocessing, gene pair

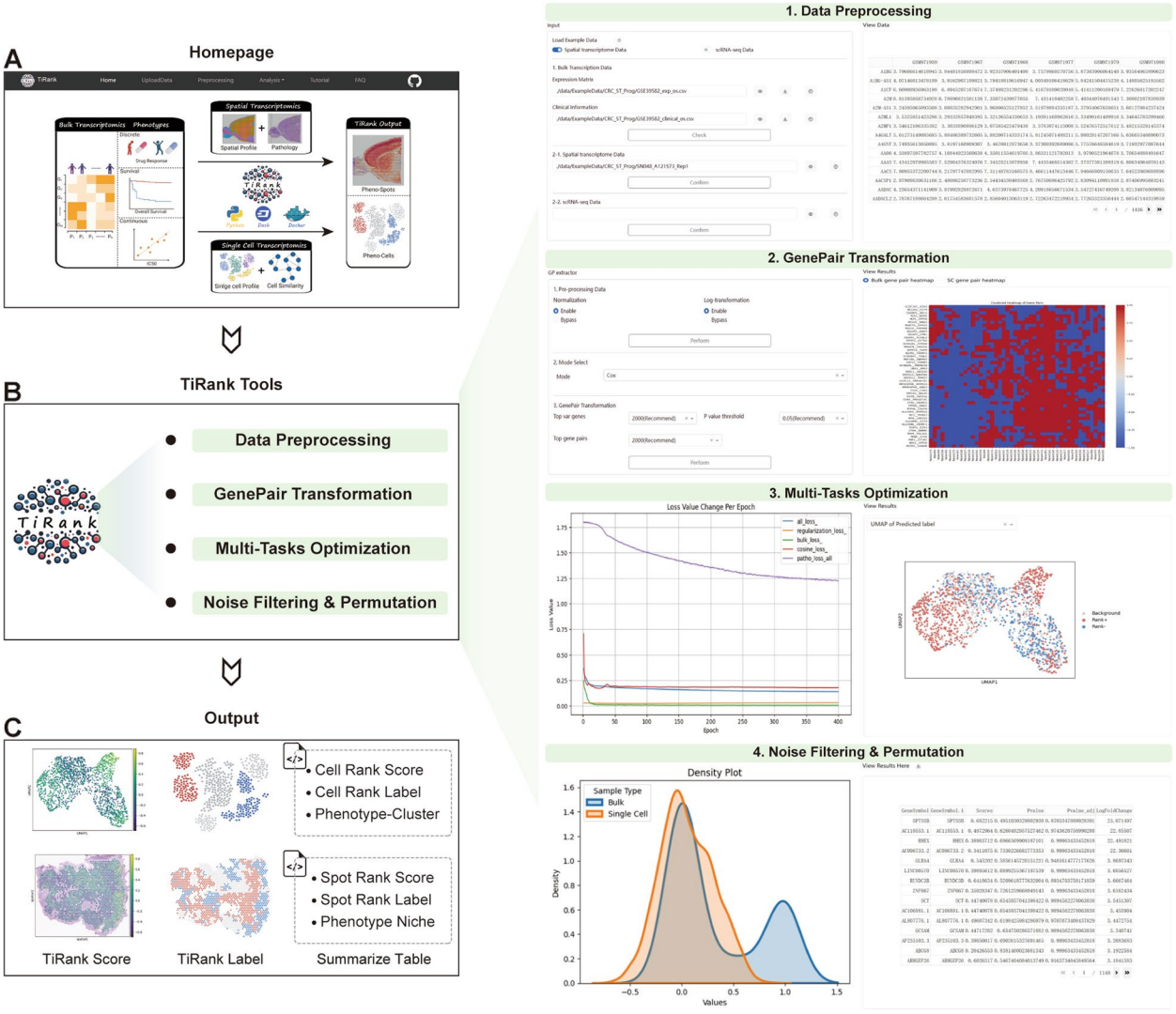

Fig. 5 Graphical user interface for TiRank. **A** Homepage of TiRank. The interface provides access to core modules for analyzing bulk transcriptomics, scRNA-seq, and ST data, with outputs linked to clinical phenotypes. **B** Overview of analysis modules in TiRank: (1) Data Preprocessing: Uploaded transcriptomics data is preprocessed, including quality control and dictionary initialization to store results. (2) REO-Transformation Module: Converts the original gene expression matrix into a REO matrix based on gene pair transformations. (3) Multitask Transfer Learning Framework: Employs multitask loss functions to infer relationships between individual cells or spots and associated phenotypes. (4) Noise Filtering and Permutation: Identifies phenotype-independent cells or spots, enabling the classification of clinical phenotype-associated subpopulations and spatial niches. **C** TiRank outputs. For scRNA-seq and ST data, TiRank provides the TiRank Score and TiRank Label, quantifying the association of cells or spatial spots with clinical phenotypes. Results are compiled into a summary table to facilitate downstream analyses

transformation, optimization, and identification of phenotype-associated cells or spots (Fig. 5B). The GUI offers multiple results and modules for downstream analysis, including a summary table presenting TiRank labels and scores that indicate associations between individual cells or spots and clinical phenotypes, a permutation algorithm for inferring clinically relevant cell subpopulations or spatial niches, and visualization and analysis modules to display results such as the distribution of TiRank labels and differentially expressed genes (Fig. 5C). A comprehensive tutorial for using the TiRank GUI is available at https://tirank.readthedocs.io/en/latest/tutorial_web.html and a video demonstration has also been added to this GitHub repository. The interactive TiRank GUI enables researchers to process their data efficiently, facilitating the discovery of clinical biomarkers.

Discussion

By integrating relative expression ordering (REO) of phenotype gene-pairs with a multitask transfer learning strategy, TiRank leverages phenotype labels available in bulk transcriptomics to prioritize phenotype-associated cells and spatial niches from scRNA-seq and ST data. Conceptually, TiRank departs from earlier frameworks such as

Scissor and DEGAS in four points. First, the REO transformation provides a modality-robust signal that reduces dependence on cross-platform expression calibration. Second, TiRank incorporates a WSI-guided location-aware module that further encourages spatial coherence for ST data. Third, TiRank introduces a GMM-based post-hoc neutral class to identify phenotype-independent cells/spots, improving interpretability in noisy clinical settings. Fourth, TiRank elevates single-cell/spot scoring to biological units via a permutation-based enrichment test for phenotype-associated subpopulations and spatial niches.

This phenotype-prioritization approach complements other spatial analysis tools. While methods like SpaGCN focus on de novo discovery of spatial domains through graph convolutional networks, and CellCharter [88] specializes in characterizing cellular composition and interactions within niches, TiRank takes a step further in systematically linking spatial structures to clinical outcomes. By transferring phenotype associations from bulk transcriptomics, TiRank directly identifies which spatial niches are clinically relevant, bridging the gap between spatial organization and patient outcomes.

Applied to GC, TiRank demonstrates potential in advancing biomarker discovery. GC remains one of the most prevalent and lethal malignancies [89]. The effectiveness of first-line chemotherapy for advanced GC is limited, with a median overall survival of less than one year [90, 91]. Although immunotherapy has been incorporated into chemotherapy regimens, only a small subset of patients could benefit from these treatments [92, 93]. In this study, we utilized TiRank to identify spatial niches within tumor boundaries that were associated with the efficacy of NACI. A novel tumor boundary region, termed "Fibro-Bar," was identified. Fibro-Bars are enriched with distinct spatial fibroblast niches, primarily composed of $MYH11^+$ CAFs, $TRPA1^+$ CAFs, $CD74^+$ CAFs, and form a barrier-like structure that contributes to the exclusion of multiple immune cell subpopulations. In our retrospective GC cohort, the Fibro-Bar Score, quantifying the relative spatial distribution of CAFs and immune cells as measured by IMC, was significantly associated with reduced responsiveness to NACI.

CAFs, which are heterogeneous and ubiquitous stromal cells within the TME, have been reported to influence the efficiency of therapy [94, 95]. Prior research indicates that activated CAFs may contribute to T-cell exclusion [96]. Specifically, $MYH11^+$ CAFs form a single-cell layer that lines tumor nests and is significantly associated with immune exclusion from tumor regions, leading to poor response to ICB in non-small cell lung cancer [65]. In this study, we further demonstrate that $MYH11^+$ CAF-derived Fibro-Bar serve as boundary-like structures that impede T-cell infiltration and limit NACI effectiveness. Furthermore, we observed upregulation of *POSTN*, *IFNγ* and *PD-1* in T and B cells within the tumor region with a high Fibro-Bar score, indicating a microenvironment characterized by epithelial-to-mesenchymal transition (EMT) and immune evasion [69].

Several limitations warrant consideration. First, TiRank leverages the REO to mitigate cross-platform scaling differences and facilitate transfer across modalities, this strategy has inherent constraints. The binarization of pairwise expression discards quantitative information, and its performance depends on adequate gene coverage, making it sensitive to technical issues like dropouts and dependent on the initial selection of phenotype-associated genes. Future extensions will explore probabilistic REO and adaptive pair selection to balance rank-based robustness with magnitude-based informativeness. Second, the GMM-based filter relies on predefined and fixed threshold. A more robustly data-driven approach would be appropriate. Third, while TiRank has demonstrated performance in predicting drug responses based on cell line data, further validation across broader and more diverse datasets, including animal models and clinical cohorts. Our benchmarking of phenotype-associated subpopulations relies on literature-derived ground truth, which may introduce selection or reporting biases, heterogeneous phenotype definitions, and variability in cell-type annotation. Although the ideal gold-standard benchmarks would consist of bulk and single-cell datasets derived from the same matched samples, together with harmonized clinical outcomes to ensure a more reliable and standardized reference, such resources are currently lacking. Finally, TiRank's applicability to spatial-omics technologies such as imaging-based ST [97] or spatial proteomics [7], remains to be evaluated. Our IMC analysis was also restricted to gastroscopic biopsies (about 1 mm^2), potentially limiting a comprehensive assessment of spatial structures, and validation in a larger, randomized prospective cohort is essential.

In summary, TiRank is a versatile deep learning model for the prioritization of clinically relevant spatial niches within the TME. Our findings indicate that Fibro-Bar serve as potential markers for guiding neoadjuvant chemoimmunotherapy in GC. To enhance accessibility, we developed an interactive graphical interface for both researchers and clinicians. We believe that TiRank offers valuable insights for clinical biomarker discovery and precision oncology.

Conclusions

TiRank is a robust deep learning framework that utilizes multitask transfer learning to integrate multimodal transcriptomics and prioritize clinically relevant spatial niches within the tumor microenvironment. Our

study highlights the "Fibro-Bar," a specific spatial niche enriched with cancer-associated fibroblasts that contributes to immune exclusion and correlates with treatment resistance in gastric cancer. The proposed novel algorithm is expected to be applicable to elucidate spatial biomarkers and guide patient-specific strategies to advance precision oncology.

Abbreviations

REO	Relative Expression Ordering
GP	Gene Pairs
PGP	Phenotypic Gene Pair
GMM	Gaussian Mixture Model
$TiRank^{+}$	A label assigned by TiRank to cells or spots positively correlated with a target phenotype (e.g., poor prognosis, therapy resistance)
$TiRank^{-}$	A label assigned by TiRank to cells or spots negatively correlated with a target phenotype (e.g., favorable prognosis, therapy response)
AML	Acute Myelogenous Leukemia
HCC	Hepatocellular Carcinoma
CRC	Colorectal Cancer
GC	Gastric Cancer
LUAD	Lung Adenocarcinoma
AC	Adjuvant Chemotherapy
ICB	Immune Checkpoint Blockade
NACI	Neo-adjuvant Chemoimmunotherapy
TRG	Tumor Regression Grade
TME	Tumor Microenvironment
CAF	Cancer-Associated Fibroblast
IMC	Imaging Mass Cytometry
scRNA-seq	Single-cell RNA Sequencing
ST	Spatial Transcriptomics
H&E	Hematoxylin and Eosin
CN	Cellular Neighborhood

Supplementary Information

The online version contains supplementary material available at https://doi.org/10.1186/s13073-026-01604-2.

Additional file 1. Description, figures of additional results and methods. Fig S1. TiRank overview and performance on drug response datasets. Fig S2. Performance evaluation of TiRank across drug response datasets. Fig S3. Visualization of TiRank scores in Drug response predictions. Fig S4. Summary of cellular subpopulations with clinical significance. Fig S5. Cellular annotation of scRNA-seq data involved for phenotype-associated cell subpopulations identification. Fig S6. Benchmarking TiRank against other algorithms in predicting prognosis-associated cell subpopulations from scRNA-seq data. Fig S7. TiRank identifies cell subpopulations associated with anti-PD-1 therapy response in melanoma. Fig S8. CD8+ T Cells associated with anti-PD1 therapy response in Melanoma. Fig S9. Benchmarking TiRank against other algorithms in predicting phenotype-associated spatial niches from CRC ST Data. Fig S10. Benchmarking TiRank against other algorithms in predicting phenotype-associated spatial niches from GC ST Data. Fig S11. TiRank identifies interactions between myofibroblasts and SPP1+ TAMs associated with prognosis in CRC. Fig S12. Co-occurrence of SPP1+ TAM and myofibroblast in poor prognostic regions in CRC. Fig S13. Spatial distributions of TiRank scores across tissue slices from CRC. Fig S14. Spatial distributions of TiRank scores across tissue slices of GC. Fig S15. Spatial characteristics of TiRank labels in GC. Fig S16. Cellular fractions at individual spots based on deconvolution analysis in GC. Fig S17. IMC images and the corresponding hematoxylin and eosin-stained images of tumor regions in GC. Fig S18. Abundance of cell subpopulations through IMC in GC. Fig S19. Cellular neighborhoods associated with TRG in GC. Fig S20. Visualization of Fibro-Bar and cell distributions through IMC. Fig S21. Features associated with the Fibro-Bar score in GC patients receiving NACI.

Additional file 2. Description, and Tables of additional results. Table S1: The datasets used in TiRank. Table S2: The collected conclusions from previous research paper for pan-cancer evaluation. Table S3: Clinical information for spatial transcriptomics data of GC. Table S4: The clinical information of UnionH-3 cohort involved in mass cytometry imaging. Table S5: Antibodies information of IMC experiments. Table S6: Selecting ROIs of IMC experiments. Table S7: Comparison of computational methods for identifying clinically relevant subpopulations or niches.

Acknowledgements
Not applicable.

Code availability
The source code for TiRank is available in the GitHub repository and has been archived in Zenodo: Yuxiang Lin, Ling Luo and Jinsheng Song. TiRank. GitHub. https://github.com/LenisLin/TiRank (2025) [98].

Authors' contributions
Y. Lin, Z. Lin, X. Li, and Y. Gao prepared the figures and drafted the manuscript. Y. Lin, Z. Huang, and Q. Chen contributed to data collection and processing. Y. Lin, Z. Lin, J. Song, Y. Lin, J. Chi, and J. Lin analyzed and interpreted the data. L. Zhang provided technical support for sequencing. Y. Lin, L. Luo, and Y. Zheng supported the construction of the graphic user interface. C. Liang, X. Wang, Y. Lin, and Z. Lin conducted the literature review. Z. Huang and Y. Sun collected the clinical cohorts. M. Tong, Q. Chen, and R. Yu conceived and reviewed the project. All authors read and approved the final manuscript.

Funding
This study was supported by the National Key R&D Program of China (grant numbers 2024YFF1206801 and 2024YFF1206800), the National Natural Science Foundation of China (grant number 82002529), the Natural Science Foundation of Fujian Province (grant number 2023J01674), the Science and Technology Innovation Joint Fund Project of Fujian Province (grant numbers 2023Y9208 and 2023Y9174), the Natural Science Foundation of Xiamen, China (grant number 3502Z202471014), the Fundamental Research Funds for the Central Universities (grant number 20720250097), Fujian Province 2025 Fiscal Special Fund (2025CZ004), and the Excellent Young Scholars Cultivation Project of Fujian Medical University Union Hospital (grant numbers 2022XH021 and 2022XH041).

Data availability
The public RNA-seq, scRNA-seq, and spatial transcriptomics datasets analyzed during the current study are available in the Gene Expression Omnibus (GEO; https://www.ncbi.nlm.nih.gov/geo/), The Cancer Genome Atlas (TCGA; https://portal.gdc.cancer.gov/), and other public repositories; specifically, cancer cell line datasets were obtained from the CCLE [99] (https://sites.broadinstitute.org/ccle/datasets) and GDSC [100] (https://pharmacodb.ca/datasets) databases as well as GEO accession numbers GSE112274, GSE117872, GSE140440, and GSE14938 [101, 102, 103, 104], while patient cohorts were sourced as follows: Non-Small Cell Lung Cancer (NSCLC) datasets from GSE126044, GSE166449, GSE33072, GSE31210, GSE37745, and GSE131907 [54, 105, 106, 107, 108, 109]; Melanoma (SKCM) datasets from published studies by Liu et al., Riaz et al., Gide et al., and Puch et al., as well as GSE120575, GSE91061, GSE78220, GSE160638, and GSE171256 [58, 59, 60, 61, 110, 111, 112, 113]; Colorectal Cancer (CRC) datasets from GSE39582, GSE14333, GSE17536, GSE33113, GSE37892, GSE235919, and GSE144735, plus spatial datasets from Alberto et al. and Wu et al. [53, 67, 68, 114, 115, 116, 117, 118, 119]; Gastric Cancer (GC) datasets from TCGA-STAD, ACRG (GSE66229), GSE15459, GSE29272, GSE34942, GSE57303, GSE26901, and GSE183904, alongside clinical cohorts from Kim et al. and Kwon et al. [57, 76, 77, 78, 79, 120, 121, 122, 123, 124]; Hepatocellular Carcinoma (HCC) datasets from GSE16174, GSE14520, GSE76427, GSE214432, GSE116174, and GSE151530 [56, 125, 126, 127, 128]; and Acute Myeloid Leukemia (AML) datasets from TCGA-LAML, Beat AML (Wave 1-4), and GSE116256 [51, 55, 129]. The accession identifiers and detailed descriptions for all public datasets are listed in Additional file 2: Table S2. The private bulk transcriptomics, spatial transcriptomics, and IMC data generated in this study have been deposited in the Zenodo database and are available in the following record: Yuxiang Lin, Zening Huang, Youxin Gao and Qiyue Chen. UnionH: A Multi-Cohort Gastric Cancer Dataset for Transcriptomics and Proteomics Analysis. Zenodo. https://doi.org/10.5281/zenodo.14864800 (2025) [130].

Declarations

Ethics approval and consent to participate

Research involving human participants was conducted in accordance with the Declaration of Helsinki. Prospective ethics approvals and written informed consent were obtained as follows: Fujian Medical University Union Hospital: Approval 2020YF013 (UnionH-1 and UnionH-2 cohorts); Zhangzhou Affiliated Hospital of Fujian Medical University: Approval 2023LWB046 (UnionH-3 cohort). All patients provided written informed consent prior to sample collection and analysis.

Consent for publication

Not applicable (no individual person's identifiable data are included).

Competing interests

The authors declare no competing interests.

Author details

[1]National Institute for Data Science in Health and Medicine, Xiamen University, Xiamen 361102, Fujian, China
[2]Department of Gastric Surgery, Fujian Medical University Union Hospital, Fuzhou 350001, Fujian, China
[3]Key Laboratory of Ministry of Education of Gastrointestinal Cancer, Fujian Medical University, Fuzhou 350001, Fujian, China
[4]State Key Laboratory of Cellular Stress Biology, School of Life Sciences, Faculty of Medicine and Life Sciences, Xiamen University, Xiamen 361102, Fujian, China
[5]School of Informatics, Xiamen University, Xiamen 361005, China
[6]Department of Gastrointestinal Surgery, Zhangzhou Affiliated Hospital of Fujian Medical University, Zhangzhou 363000, China

Received: 23 May 2025 / Accepted: 27 January 2026
Published online: 13 February 2026

References

1. Bejarano L, Jordão MJC, Joyce JA. Therapeutic targeting of the tumor microenvironment. Cancer Discov. 2021;11:933–59. https://doi.org/10.1158/2159-8290.CD-20-1808.
2. Visser KEde, Joyce JA. The evolving tumor microenvironment: from cancer initiation to metastatic outgrowth. Cancer Cell. 2023;41:374–403. https://doi.org/10.1016/j.ccell.2023.02.016.
3. Bruni D, Angell HK, Galon J. The immune contexture and Immunoscore in cancer prognosis and therapeutic efficacy. Nat Rev Cancer. 2020;20:662–80. https://doi.org/10.1038/s41568-020-0285-7.
4. Tang T, Huang X, Zhang G, Hong Z, Bai X, Liang T. Advantages of targeting the tumor immune microenvironment over blocking immune checkpoint in cancer immunotherapy. Signal Transduct Target Ther. 2021;6:72. https://doi.org/10.1038/s41392-020-00449-4.
5. Lim B, Lin Y, Navin N. Advancing cancer research and medicine with single-cell genomics. Cancer Cell. 2020;37:456–70. https://doi.org/10.1016/j.ccell.2020.03.008.
6. Lei Y, Tang R, Xu J, Wang W, Zhang B, Liu J, et al. Applications of single-cell sequencing in cancer research: progress and perspectives. J Hematol Oncol. 2021;14:91. https://doi.org/10.1186/s13045-021-01105-2.
7. de Souza N, Zhao S, Bodenmiller B. Multiplex protein imaging in tumour biology. Nat Rev Cancer. 2024;24:171–91. https://doi.org/10.1038/s41568-023-00657-4.
8. Liu Y, Xun Z, Ma K, Liang S, Li X, Zhou S, et al. Identification of a tumour immune barrier in the HCC microenvironment that determines the efficacy of immunotherapy. J Hepatol. 2023;78:770–82. https://doi.org/10.1016/j.jhep.2023.01.011.
9. You S, Li S, Zeng L, Song J, Li Z, Li W, et al. Lymphatic-localized Treg-mregDC crosstalk limits antigen trafficking and restrains anti-tumor immunity. Cancer Cell. 2024;S1535–6108(24):00239–43. https://doi.org/10.1016/j.ccell.2024.06.014.
10. Chen J, Larsson L, Swarbrick A, Lundeberg J. Spatial landscapes of cancers: insights and opportunities. Nat Rev Clin Oncol. 2024. https://doi.org/10.1038/s41571-024-00926-7.
11. Zhi Y, Wang Q, Zi M, Zhang S, Ge J, Liu K, et al. Spatial Transcriptomic and Metabolomic Landscapes of Oral Submucous Fibrosis-Derived Oral Squamous Cell Carcinoma and its Tumor Microenvironment. Adv Sci (Weinh). 2024;e2306515. https://doi.org/10.1002/advs.202306515
12. Zhang Y, Liu G, Zeng Q, Wu W, Lei K, Zhang C, et al. Ccl19-producing fibroblasts promote tertiary lymphoid structure formation enhancing anti-tumor IgG response in colorectal cancer liver metastasis. Cancer Cell. 2024;42:1370-1385.e9. https://doi.org/10.1016/j.ccell.2024.07.006.
13. Hao Y, Stuart T, Kowalski MH, Choudhary S, Hoffman P, Hartman A, et al. Dictionary learning for integrative, multimodal and scalable single-cell analysis. Nat Biotechnol Nature Publishing Group. 2024;42:293–304. https://doi.org/10.1038/s41587-023-01767-y.
14. Wolf FA, Angerer P, Theis FJ. SCANPY: large-scale single-cell gene expression data analysis. Genome Biol. 2018;19:15. https://doi.org/10.1186/s13059-017-1382-0.
15. Ren T, Chen C, Danilov AV, Liu S, Guan X, Du S, et al. Supervised learning of high-confidence phenotypic subpopulations from single-cell data. Nat Mach Intell. 2023;5:528–41. https://doi.org/10.1038/s42256-023-00656-y.
16. Xu Z, Wang W, Yang T, Li L, Ma X, Chen J, et al. STOmicsDB: a comprehensive database for spatial transcriptomics data sharing, analysis and visualization. Nucleic Acids Res. 2023. https://doi.org/10.1093/nar/gkad933.
17. Sun D, Guan X, Moran AE, Wu L-Y, Qian DZ, Schedin P, et al. Identifying phenotype-associated subpopulations by integrating bulk and single-cell sequencing data. Nat Biotechnol. 2022;40:527–38. https://doi.org/10.1038/s41587-021-01091-3.
18. Johnson TS, Yu CY, Huang Z, Xu S, Wang T, Dong C, et al. Diagnostic evidence gauge of single cells (DEGAS): a flexible deep transfer learning framework for prioritizing cells in relation to disease. Genome Med. 2022;14:11. https://doi.org/10.1186/s13073-022-01012-2.
19. Chen J, Wang X, Ma A, Wang QE, Liu B, Li L, et al. Deep transfer learning of cancer drug responses by integrating bulk and single-cell RNA-seq data. Nat Commun. 2022;13:6494. https://doi.org/10.1038/s41467-022-34277-7.
20. Colaprico A, Silva TC, Olsen C, Garofano L, Cava C, Garolini D, et al. TCGAbiolinks: an R/Bioconductor package for integrative analysis of TCGA data. Nucleic Acids Res. 2016;44:e71. https://doi.org/10.1093/nar/gkv1507.
21. Liu Y, Lin Y, Yang W, Lin Y, Wu Y, Zhang Z, et al. Application of individualized differential expression analysis in human cancer proteome. Brief Bioinform. 2022;23:bbac096. https://doi.org/10.1093/bib/bbac096.
22. Tong M, Lin Y, Yang W, Song J, Zhang Z, Xie J, et al. Prioritizing prognostic-associated subpopulations and individualized recurrence risk signatures from single-cell transcriptomes of colorectal cancer. Brief Bioinform. 2023;24:bbad078. https://doi.org/10.1093/bib/bbad078.
23. Hu J, Li X, Coleman K, Schroeder A, Ma N, Irwin DJ, et al. SpaGCN: integrating gene expression, spatial location and histology to identify spatial domains and spatially variable genes by graph convolutional network. Nat Methods. 2021;18:1342–51. https://doi.org/10.1038/s41592-021-01255-8.
24. Li H, Zhou J, Li Z, Chen S, Liao X, Zhang B, et al. A comprehensive benchmarking with practical guidelines for cellular deconvolution of spatial transcriptomics. Nat Commun. 2023;14:1548. https://doi.org/10.1038/s41467-023-37168-7.
25. Li B, Cui Y, Diehn M, Li R. Development and validation of an individualized immune prognostic signature in early-stage nonsquamous non-small cell lung cancer. JAMA Oncol. 2017;3:1529–37. https://doi.org/10.1001/jamaoncol.2017.1609.
26. Heinäniemi M, Nykter M, Kramer R, Wienecke-Baldacchino A, Sinkkonen L, Zhou JX, et al. Gene-pair expression signatures reveal lineage control. Nat Methods. 2013;10:577–83. https://doi.org/10.1038/nmeth.2445.
27. Xu C, Jin X, Wei S, Wang P, Luo M, Xu Z, et al. DeepST: identifying spatial domains in spatial transcriptomics by deep learning. Nucleic Acids Res. 2022;50:e131. https://doi.org/10.1093/nar/gkac901.
28. Wang X, Yang S, Zhang J, Wang M, Zhang J, Yang W, et al. Transformer-based unsupervised contrastive learning for histopathological image classification. Med Image Anal. 2022;81:102559. https://doi.org/10.1016/j.media.2022.102559.
29. Boluki S, Esfahani MS, Qian X, Dougherty ER. Constructing pathway-based priors within a Gaussian mixture model for Bayesian regression and classification. IEEE ACM Trans Comput Biol Bioinform. 2019;16:524–37. https://doi.org/10.1109/TCBB.2017.2778715.
30. Akiba T, Sano S, Yanase T, Ohta T, Koyama M. Optuna: a next-generation hyperparameter optimization framework. arXiv; 2019. https://doi.org/10.48550/arXiv.1907.10902. Cited 2026 Jan 19.
31. Chawla NV, Bowyer KW, Hall LO, Kegelmeyer WP. SMOTE: synthetic minority over-sampling technique. J Artif Intell Res. 2002;16:321–57. https://doi.org/10.1613/jair.953.

32. Fustero-Torre C, Jiménez-Santos MJ, García-Martín S, Carretero-Puche C, García-Jimeno L, Ivanchuk V, et al. Beyondcell: targeting cancer therapeutic heterogeneity in single-cell RNA-seq data. Genome Med. 2021;13:187. https://doi.org/10.1186/s13073-021-01001-x.
33. Chomczynski P, Sacchi N. Single-step method of RNA isolation by acid guanidinium thiocyanate-phenol-chloroform extraction. Anal Biochem. 1987;162:156–9. https://doi.org/10.1006/abio.1987.9999.
34. Xun Z, Ding X, Zhang Y, Zhang B, Lai S, Zou D, et al. Reconstruction of the tumor spatial microenvironment along the malignant-boundary-nonmalignant axis. Nat Commun. 2023;14:933. https://doi.org/10.1038/s41467-023-36560-7.
35. Ma Y, Zhou X. Spatially informed cell-type deconvolution for spatial transcriptomics. Nat Biotechnol. 2022;40:1349–59. https://doi.org/10.1038/s41587-022-01273-7.
36. Tanevski J, Flores ROR, Gabor A, Schapiro D, Saez-Rodriguez J. Explainable multiview framework for dissecting spatial relationships from highly multiplexed data. Genome Biol. 2022;23:97. https://doi.org/10.1186/s13059-022-02663-5.
37. Windhager J, Zanotelli VRT, Schulz D, Meyer L, Daniel M, Bodenmiller B, et al. An end-to-end workflow for multiplexed image processing and analysis. Nat Protoc. 2023;18:3565–613. https://doi.org/10.1038/s41596-023-00881-0.
38. Greenwald NF, Miller G, Moen E, Kong A, Kagel A, Dougherty T, et al. Whole-cell segmentation of tissue images with human-level performance using large-scale data annotation and deep learning. Nat Biotechnol Nature Publishing Group. 2022;40:555–65. https://doi.org/10.1038/s41587-021-01094-0.
39. Xiao X, Guo Q, Cui C, Lin Y, Zhang L, Ding X, et al. Multiplexed imaging mass cytometry reveals distinct tumor-immune microenvironments linked to immunotherapy responses in melanoma. Commun Med. 2022;2:131. https://doi.org/10.1038/s43856-022-00197-2.
40. Van Gassen S, Callebaut B, Van Helden MJ, Lambrecht BN, Demeester P, Dhaene T, et al. FlowSOM: using self-organizing maps for visualization and interpretation of cytometry data. Cytometry A. 2015;87:636–45. https://doi.org/10.1002/cyto.a.22625.
41. Goltsev Y, Samusik N, Kennedy-Darling J, Bhate S, Hale M, Vazquez G, et al. Deep profiling of Mouse splenic architecture with CODEX multiplexed imaging. Cell. 2018;174:968-981.e15. https://doi.org/10.1016/j.cell.2018.07.010.
42. Schapiro D, Jackson HW, Raghuraman S, Fischer JR, Zanotelli VRT, Schulz D, et al. HistoCAT: analysis of cell phenotypes and interactions in multiplex image cytometry data. Nat Methods. 2017;14:873–6. https://doi.org/10.1038/nmeth.4391.
43. Hoch T, Schulz D, Eling N, Gómez JM, Levesque MP, Bodenmiller B. Multiplexed imaging mass cytometry of the chemokine milieus in melanoma characterizes features of the response to immunotherapy. Sci Immunol. 2022;7:eabk1692. https://doi.org/10.1126/sciimmunol.abk1692.
44. Subramanian A, Tamayo P, Mootha VK, Mukherjee S, Ebert BL, Gillette MA, et al. Gene set enrichment analysis: a knowledge-based approach for interpreting genome-wide expression profiles. Proc Natl Acad Sci U S A. 2005;102:15545–50. https://doi.org/10.1073/pnas.0506580102.
45. Qiu X, Hill A, Packer J, Lin D, Ma Y-A, Trapnell C. Single-cell mRNA quantification and differential analysis with Census. Nat Methods. 2017;14:309–15. https://doi.org/10.1038/nmeth.4150.
46. Vandereyken K, Sifrim A, Thienpont B, Voet T. Methods and applications for single-cell and spatial multi-omics. Nat Rev Genet. 2023;24:494–515. https://doi.org/10.1038/s41576-023-00580-2.
47. Cancer Cell Line Encyclopedia Consortium, Genomics of Drug Sensitivity in Cancer Consortium. Pharmacogenomic agreement between two cancer cell line data sets. Nature. 2015;528:84–7. https://doi.org/10.1038/nature15736.
48. Huang G, Liu Z, van der Maaten L, Weinberger KQ. Densely connected convolutional networks. arXiv. 2018. https://doi.org/10.48550/arXiv.1608.06993.
49. Vaswani A, Shazeer N, Parmar N, Uszkoreit J, Jones L, Gomez AN, et al. Attention is All you Need. Advances in Neural Information Processing Systems. Curran Associates, Inc.; 2017 [cited 2025 Apr 29]. https://proceedings.neurips.cc/paper/2017/hash/3f5ee243547dee91fbd053c1c4a845aa-Abstract.html. Accessed 29 Apr 2025
50. Sinha S, Vegesna R, Mukherjee S, Kammula AV, Dhruba SR, Wu W, et al. PERCEPTION predicts patient response and resistance to treatment using single-cell transcriptomics of their tumors. Nat Cancer. 2024. https://doi.org/10.1038/s43018-024-00756-7.
51. Bottomly D, Long N, Schultz AR, Kurtz SE, Tognon CE, Johnson K, et al. Integrative analysis of drug response and clinical outcome in acute myeloid leukemia. Cancer Cell. 2022;40:850-864.e9. https://doi.org/10.1016/j.ccell.2022.07.002.
52. Newman AM, Liu CL, Green MR, Gentles AJ, Feng W, Xu Y, et al. Robust enumeration of cell subsets from tissue expression profiles. Nat Methods. 2015;12:453–7. https://doi.org/10.1038/nmeth.3337.
53. Lee HO, Hong Y, Etlioglu HE, Cho YB, Pomella V, Van den Bosch B, et al. Lineage-dependent gene expression programs influence the immune landscape of colorectal cancer. Nat Genet. 2020;52:594–603. https://doi.org/10.1038/s41588-020-0636-z.
54. Kim N, Kim HK, Lee K, Hong Y, Cho JH, Choi JW, et al. Single-cell RNA sequencing demonstrates the molecular and cellular reprogramming of metastatic lung adenocarcinoma. Nat Commun. 2020;11:2285. https://doi.org/10.1038/s41467-020-16164-1.
55. van Galen P, Hovestadt V, Wadsworth Ii MH, Hughes TK, Griffin GK, Battaglia S, et al. Single-Cell RNA-Seq Reveals AML hierarchies relevant to disease progression and immunity. Cell. 2019;176:1265-1281.e24. https://doi.org/10.1016/j.cell.2019.01.031.
56. Ma L, Wang L, Khatib SA, Chang C-W, Heinrich S, Dominguez DA, et al. Single-cell atlas of tumor cell evolution in response to therapy in hepatocellular carcinoma and intrahepatic cholangiocarcinoma. J Hepatol. 2021;75:1397–408. https://doi.org/10.1016/j.jhep.2021.06.028.
57. Kumar V, Ramnarayanan K, Sundar R, Padmanabhan N, Srivastava S, Koiwa M, et al. Single-cell atlas of lineage states, tumor microenvironment, and subtype-specific expression programs in gastric cancer. Cancer Discov. 2022;12:670–91. https://doi.org/10.1158/2159-8290.CD-21-0683.
58. Sade-Feldman M, Yizhak K, Bjorgaard SL, Ray JP, de Boer CG, Jenkins RW, et al. Defining T cell states associated with response to checkpoint immunotherapy in melanoma. Cell. 2019;176:404. https://doi.org/10.1016/j.cell.2018.12.034.
59. Cui C, Xu C, Yang W, Chi Z, Sheng X, Si L, et al. Ratio of the interferon-γ signature to the immunosuppression signature predicts anti-PD-1 therapy response in melanoma. NPJ Genom Med. 2021;6:7. https://doi.org/10.1038/s41525-021-00169-w.
60. Riaz N, Havel JJ, Makarov V, Desrichard A, Urba WJ, Sims JS, et al. Tumor and microenvironment evolution during immunotherapy with nivolumab. Cell. 2017;171:934-949 e16. https://doi.org/10.1016/j.cell.2017.09.028.
61. Gide TN, Quek C, Menzies AM, Tasker AT, Shang P, Holst J, et al. Distinct immune cell populations define response to anti-PD-1 monotherapy and anti-PD-1/anti-CTLA-4 combined therapy. Cancer Cell. 2019;35:238-255.e6. https://doi.org/10.1016/j.ccell.2019.01.003.
62. Chu Y, Dai E, Li Y, Han G, Pei G, Ingram DR, et al. Pan-cancer T cell atlas links a cellular stress response state to immunotherapy resistance. Nat Med. 2023;29:1550–62. https://doi.org/10.1038/s41591-023-02371-y.
63. Xu H, Zhang A, Fang C, Zhu Q, Wang W, Liu Y, et al. *SLC11A1* as a stratification indicator for immunotherapy or chemotherapy in patients with glioma. Front Immunol. 2022;13:980378. https://doi.org/10.3389/fimmu.2022.980378.
64. Thommen DS, Koelzer VH, Herzig P, Roller A, Trefny M, Dimeloe S, et al. A transcriptionally and functionally distinct PD-1+ CD8+ T cell pool with predictive potential in non-small-cell lung cancer treated with PD-1 blockade. Nat Med. 2018;24:994–1004. https://doi.org/10.1038/s41591-018-0057-z.
65. Hu Y, Rong J, Xu Y, Xie R, Peng J, Gao L, et al. Unsupervised and supervised discovery of tissue cellular neighborhoods from cell phenotypes. Nat Methods. 2024. https://doi.org/10.1038/s41592-023-02124-2.
66. Cui Y, Yuan Z. Scalable Condition-relevant Cell Niche Analysis of Spatial Omics Data with Taichi. bioRxiv; 2024. p. 2024.05.30.596656. https://doi.org/10.1101/2024.05.30.596656. Cited 2025 Apr 28.
67. Valdeolivas A, Amberg B, Giroud N, Richardson M, Gálvez EJC, Badillo S, et al. Profiling the heterogeneity of colorectal cancer consensus molecular subtypes using spatial transcriptomics. npj Precis Onc. Nature Publishing Group; 2024;8:1–16. https://doi.org/10.1038/s41698-023-00488-4
68. Wu Y, Yang S, Ma J, Chen Z, Song G, Rao D, et al. Spatiotemporal immune landscape of colorectal cancer liver metastasis at single-cell level. Cancer Discov. 2022;12:134–53. https://doi.org/10.1158/2159-8290.CD-21-0316.
69. Wang Z, Wang B, Feng Y, Ye J, Mao Z, Zhang T, et al. Targeting tumor-associated macrophage-derived CD74 improves efficacy of neoadjuvant chemotherapy in combination with PD-1 blockade for cervical cancer. J Immunother Cancer. 2024;12:e009024. https://doi.org/10.1136/jitc-2024-009024.
70. Gao Y, Li J, Cheng W, Diao T, Liu H, Bo Y, et al. Cross-tissue human fibroblast atlas reveals myofibroblast subtypes with distinct roles in immune modulation. Cancer Cell. 2024;S1535–6108(24):00319–22. https://doi.org/10.1016/j.ccell.2024.08.020.
71. Chhabra Y, Weeraratna AT. Fibroblasts in cancer: unity in heterogeneity. Cell. 2023;186:1580–609. https://doi.org/10.1016/j.cell.2023.03.016.

72. Propper DJ, Balkwill FR. Harnessing cytokines and chemokines for cancer therapy. Nat Rev Clin Oncol. 2022;19:237–53. https://doi.org/10.1038/s41571-021-00588-9.
73. Huangfu L, Li R, Huang Y, Wang S. The IL-17 family in diseases: from bench to bedside. Signal Transduct Target Ther. 2023;8:402. https://doi.org/10.1038/s41392-023-01620-3.
74. Qi J, Sun H, Zhang Y, Wang Z, Xun Z, Li Z, et al. Single-cell and spatial analysis reveal interaction of FAP+ fibroblasts and SPP1+ macrophages in colorectal cancer. Nat Commun. 2022;13:1742. https://doi.org/10.1038/s41467-022-29366-6.
75. Mayer S, Milo T, Isaacson A, Halperin C, Miyara S, Stein Y, et al. The tumor microenvironment shows a hierarchy of cell-cell interactions dominated by fibroblasts. Nat Commun. 2023;14:5810. https://doi.org/10.1038/s41467-023-41518-w.
76. Oh SC, Sohn BH, Cheong J-H, Kim S-B, Lee JE, Park KC, et al. Clinical and genomic landscape of gastric cancer with a mesenchymal phenotype. Nat Commun. 2018;9:1777. https://doi.org/10.1038/s41467-018-04179-8.
77. Kim ST, Cristescu R, Bass AJ, Kim K-M, Odegaard JI, Kim K, et al. Comprehensive molecular characterization of clinical responses to PD-1 inhibition in metastatic gastric cancer. Nat Med. 2018;24:1449–58. https://doi.org/10.1038/s41591-018-0101-z.
78. Kwon M, An M, Klempner SJ, Lee H, Kim K-M, Sa JK, et al. Determinants of response and intrinsic resistance to PD-1 blockade in microsatellite instability-high gastric cancer. Cancer Discov. 2021;11:2168–85. https://doi.org/10.1158/2159-8290.CD-21-0219.
79. Cristescu R, Lee J, Nebozhyn M, Kim K-M, Ting JC, Wong SS, et al. Molecular analysis of gastric cancer identifies subtypes associated with distinct clinical outcomes. Nat Med. 2015;21:449–56. https://doi.org/10.1038/nm.3850.
80. Wu Z, Bezwada D, Cai F, Harris RC, Ko B, Sondhi V, et al. Electron transport chain inhibition increases cellular dependence on purine transport and salvage. Cell Metab. 2024;36:1504-1520.e9. https://doi.org/10.1016/j.cmet.2024.05.014.
81. Luo H, Xia X, Huang L-B, An H, Cao M, Kim GD, et al. Pan-cancer single-cell analysis reveals the heterogeneity and plasticity of cancer-associated fibroblasts in the tumor microenvironment. Nat Commun. 2022;13:6619. https://doi.org/10.1038/s41467-022-34395-2.
82. Grout JA, Sirven P, Leader AM, Maskey S, Hector E, Puisieux I, et al. Spatial positioning and matrix programs of cancer-associated fibroblasts promote T-cell exclusion in human lung tumors. Cancer Discov. 2022;12:2606–25. https://doi.org/10.1158/2159-8290.CD-21-1714.
83. Geng P, Ye F, Dou P, Hu C, He J, Zhao J, et al. HIF-1α-HPRT1 axis promotes tumorigenesis and gefitinib resistance by enhancing purine metabolism in EGFR-mutant lung adenocarcinoma. J Exp Clin Cancer Res. 2024;43:269. https://doi.org/10.1186/s13046-024-03184-8.
84. Barbetta A, Rocque B, Bangerth S, Street K, Weaver C, Chopra S, et al. Spatially resolved immune exhaustion within the alloreactive microenvironment predicts liver transplant rejection. Sci Adv. 2024;10:eadm8841. https://doi.org/10.1126/sciadv.adm8841.
85. Cao LL, Lu H, Soutto M, Bhat N, Chen Z, Peng D, et al. Multivalent tyrosine kinase inhibition promotes T cell recruitment to immune-desert gastric cancers by restricting epithelial-mesenchymal transition via tumour-intrinsic IFN-γ signalling. Gut. 2023;72:2038–50. https://doi.org/10.1136/gutjnl-2022-329134.
86. Holzgruber J, Martins C, Kulcsar Z, Duplaine A, Rasbach E, Migayron L, et al. Type I interferon signaling induces melanoma cell-intrinsic PD-1 and its inhibition antagonizes immune checkpoint blockade. Nat Commun. 2024;15:7165. https://doi.org/10.1038/s41467-024-51496-2.
87. Enfield KSS, Colliver E, Lee C, Magness A, Moore DA, Sivakumar M, et al. Spatial architecture of myeloid and T cells orchestrates immune evasion and clinical outcome in lung cancer. Cancer Discov. 2024;14:1018–47. https://doi.org/10.1158/2159-8290.CD-23-1380.
88. Varrone M, Tavernari D, Santamaria-Martínez A, Walsh LA, Ciriello G. CellCharter reveals spatial cell niches associated with tissue remodeling and cell plasticity. Nat Genet. 2024;56:74–84. https://doi.org/10.1038/s41588-023-01588-4.
89. Siegel RL, Kratzer TB, Giaquinto AN, Sung H, Jemal A. Cancer statistics, 2025. CA Cancer J Clin. 2025;75:10–45. https://doi.org/10.3322/caac.21871.
90. Janjigian YY, Shitara K, Moehler M, Garrido M, Salman P, Shen L, et al. First-line nivolumab plus chemotherapy versus chemotherapy alone for advanced gastric, gastro-oesophageal junction, and oesophageal adenocarcinoma (CheckMate 649): a randomised, open-label, phase 3 trial. Lancet. 2021;398:27–40. https://doi.org/10.1016/S0140-6736(21)00797-2.
91. Catenacci DVT, Tebbutt NC, Davidenko I, Murad AM, Al-Batran S-E, Ilson DH, et al. Rilotumumab plus epirubicin, cisplatin, and capecitabine as first-line therapy in advanced MET-positive gastric or gastro-oesophageal junction cancer (RILOMET-1): a randomised, double-blind, placebo-controlled, phase 3 trial. Lancet Oncol. 2017;18:1467–82. https://doi.org/10.1016/S1470-2045(17)30566-1.
92. Fong C, Cunningham D. Chemotherapy with nivolumab in advanced gastro-oesophageal adenocarcinoma. Lancet. 2021;398:2–3. https://doi.org/10.1016/S0140-6736(21)00988-0.
93. Kang YK, Chen LT, Ryu MH, Oh DY, Oh SC, Chung HC, et al. Nivolumab plus chemotherapy versus placebo plus chemotherapy in patients with HER2-negative, untreated, unresectable advanced or recurrent gastric or gastro-oesophageal junction cancer (ATTRACTION-4): a randomised, multicentre, double-blind, placebo-controlled, phase 3 trial. Lancet Oncol. 2022;23:234–47. https://doi.org/10.1016/S1470-2045(21)00692-6.
94. Jing S-Y, Liu D, Feng N, Dong H, Wang H-Q, Yan X, et al. Spatial multiomics reveals a subpopulation of fibroblasts associated with cancer stemness in human hepatocellular carcinoma. Genome Med. 2024;16:98. https://doi.org/10.1186/s13073-024-01367-8.
95. Cords L, de Souza N, Bodenmiller B. Classifying cancer-associated fibroblasts-the good, the bad, and the target. Cancer Cell. 2024;42:1480–5. https://doi.org/10.1016/j.ccell.2024.08.011.
96. Mariathasan S, Turley SJ, Nickles D, Castiglioni A, Yuen K, Wang Y, et al. TGFβ attenuates tumour response to PD-L1 blockade by contributing to exclusion of T cells. Nature. 2018;554:544–8. https://doi.org/10.1038/nature25501.
97. Liu C, Xie J, Lin B, Tian W, Wu Y, Xin S, et al. Pan-cancer single-cell and spatial-resolved profiling reveals the immunosuppressive role of APOE+ macrophages in immune checkpoint inhibitor therapy. Adv Sci (Weinh). 2024;11:2401061. https://doi.org/10.1002/advs.202401061.
98. LenisLin. LenisLin/TiRank. 2026 [cited 2026 Jan 19]. https://github.com/LenisLin/TiRank. Accessed 19 Jan 2026
99. Barretina J, Caponigro G, Stransky N, Venkatesan K, Margolin AA, Kim S, et al. The Cancer Cell Line Encyclopedia enables predictive modelling of anticancer drug sensitivity. Datasets. Cancer Cell Line Encyclopedia. https://doi.org/10.1038/nature11003(2012).
100. Yang W, Soares J, Greninger P, Edelman EJ, Lightfoot H, Forbes S, et al. Genomics of Drug Sensitivity in Cancer (GDSC): a resource for therapeutic biomarker discovery in cancer cells. Datasets. Genomics of Drug Sensitivity in Cancer. https://doi.org/10.1093/nar/gks1111(2013).
101. Kong SL, Li H, Tai JA, Courtois ET, Poh HM, Lau DP, et al. Concurrent single-cell RNA and targeted DNA sequencing on an automated platform for comeasurement of genomic and transcriptomic signatures. Clin Chem. 2019;65:272–81. https://doi.org/10.1373/clinchem.2018.295717.
102. Ravasio A, Myaing MZ, Chia S, Arora A, Sathe A, Cao EY, et al. Single-cell analysis of EphA clustering phenotypes to probe cancer cell heterogeneity. Commun Biol. 2020;3:429. https://doi.org/10.1038/s42003-020-01136-4.
103. Schnepp PM, Shelley G, Dai J, Wakim N, Jiang H, Mizokami A, et al. Single-cell transcriptomics analysis identifies nuclear protein 1 as a regulator of docetaxel resistance in prostate cancer cells. Mol Cancer Res. 2020;18:1290–301. https://doi.org/10.1158/1541-7786.MCR-20-0051.
104. Aissa AF, Islam ABMMK, Ariss MM, Go CC, Rader AE, Conrardy RD, et al. Single-cell transcriptional changes associated with drug tolerance and response to combination therapies in cancer. Nat Commun. 2021;12:1628. https://doi.org/10.1038/s41467-021-21884-z.
105. Cho J-W, Hong MH, Ha S-J, Kim Y-J, Cho BC, Lee I, et al. Genome-wide identification of differentially methylated promoters and enhancers associated with response to anti-PD-1 therapy in non-small cell lung cancer. Exp Mol Med. 2020;52:1550–63. https://doi.org/10.1038/s12276-020-00493-8.
106. Lee JS, Nair NU, Dinstag G, Chapman L, Chung Y, Wang K, et al. Synthetic lethality-mediated precision oncology via the tumor transcriptome. Cell. 2021;184:2487-2502.e13. https://doi.org/10.1016/j.cell.2021.03.030.
107. Byers LA, Diao L, Wang J, Saintigny P, Girard L, Peyton M, et al. An epithelial-mesenchymal transition gene signature predicts resistance to EGFR and PI3K inhibitors and identifies Axl as a therapeutic target for overcoming EGFR inhibitor resistance. Clin Cancer Res. 2013;19:279–90. https://doi.org/10.1158/1078-0432.CCR-12-1558.
108. Yamauchi M, Yamaguchi R, Nakata A, Kohno T, Nagasaki M, Shimamura T, et al. Epidermal growth factor receptor tyrosine kinase defines critical prognostic genes of stage I lung adenocarcinoma. PLoS ONE. 2012;7:e43923. https://doi.org/10.1371/journal.pone.0043923.
109. Botling J, Edlund K, Lohr M, Hellwig B, Holmberg L, Lambe M, et al. Biomarker discovery in non-small cell lung cancer: integrating gene expression

profiling, meta-analysis, and tissue microarray validation. Clin Cancer Res. 2013;19:194–204. https://doi.org/10.1158/1078-0432.CCR-12-1139.
110. Li C, Phoon YP, Karlinsey K, Tian YF, Thapaliya S, Thongkum A, et al. A high OXPHOS CD8 T cell subset is predictive of immunotherapy resistance in melanoma patients. J Exp Med. 2022;219:e20202084. https://doi.org/10.1084/jem.20202084.
111. Hugo W, Zaretsky JM, Sun L, Song C, Moreno BH, Hu-Lieskovan S, et al. Genomic and transcriptomic features of response to anti-PD-1 therapy in metastatic melanoma. Cell. 2016;165:35–44. https://doi.org/10.1016/j.cell.2016.02.065.
112. Liu D, Schilling B, Liu D, Sucker A, Livingstone E, Jerby-Arnon L, et al. Integrative molecular and clinical modeling of clinical outcomes to PD1 blockade in patients with metastatic melanoma. Nat Med. 2019;25:1916–27. https://doi.org/10.1038/s41591-019-0654-5.
113. Markovits E, Harush O, Baruch EN, Shulman ED, Debby A, Itzhaki O, et al. MYC induces immunotherapy and IFNγ resistance through downregulation of JAK2. Cancer Immunol Res. 2023;11:909–24. https://doi.org/10.1158/2326-6066.CIR-22-0184.
114. de Sousa E, Melo F, Colak S, Buikhuisen J, Koster J, Cameron K, et al. Methylation of cancer-stem-cell-associated Wnt target genes predicts poor prognosis in colorectal cancer patients. Cell Stem Cell. 2011;9:476–85. https://doi.org/10.1016/j.stem.2011.10.008.
115. Smith JJ, Deane NG, Wu F, Merchant NB, Zhang B, Jiang A, et al. Experimentally derived metastasis gene expression profile predicts recurrence and death in patients with colon cancer. Gastroenterology. 2010;138:958–68. https://doi.org/10.1053/j.gastro.2009.11.005.
116. Jorissen RN, Gibbs P, Christie M, Prakash S, Lipton L, Desai J, et al. Metastasis-associated gene expression changes predict poor outcomes in patients with Dukes stage B and C colorectal cancer. Clin Cancer Res. 2009;15:7642–51. https://doi.org/10.1158/1078-0432.CCR-09-1431.
117. Marisa L, de Reyniès A, Duval A, Selves J, Gaub MP, Vescovo L, et al. Gene expression classification of colon cancer into molecular subtypes: characterization, validation, and prognostic value. PLoS Med. 2013;10:e1001453. https://doi.org/10.1371/journal.pmed.1001453.
118. Thibaudin M, Fumet JD, Chibaudel B, Bennouna J, Borg C, Martin-Babau J, et al. First-line durvalumab and tremelimumab with chemotherapy in RAS-mutated metastatic colorectal cancer: a phase 1b/2 trial. Nat Med. 2023. https://doi.org/10.1038/s41591-023-02497-z.
119. Laibe S, Lagarde A, Ferrari A, Monges G, Birnbaum D, Olschwang S. A seven-gene signature aggregates a subgroup of stage II colon cancers with stage III. OMICS. 2012;16:560–5. https://doi.org/10.1089/omi.2012.0039.
120. Planche A, Bacac M, Provero P, Fusco C, Delorenzi M, Stehle J-C, et al. Identification of prognostic molecular features in the reactive stroma of human breast and prostate cancer. PLoS ONE. 2011;6:e18640. https://doi.org/10.1371/journal.pone.0018640.
121. Ooi CH, Ivanova T, Wu J, Lee M, Tan IB, Tao J, et al. Oncogenic pathway combinations predict clinical prognosis in gastric cancer. PLoS Genet. 2009;5:e1000676. https://doi.org/10.1371/journal.pgen.1000676.
122. Cancer Genome Atlas Research Network. Comprehensive molecular characterization of gastric adenocarcinoma. Nature. 2014;513:202–9. https://doi.org/10.1038/nature13480.
123. Chia N-Y, Deng N, Das K, Huang D, Hu L, Zhu Y, et al. Regulatory crosstalk between lineage-survival oncogenes KLF5, GATA4 and GATA6 cooperatively promotes gastric cancer development. Gut. 2015;64:707–19. https://doi.org/10.1136/gutjnl-2013-306596.
124. Qian Z, Zhu G, Tang L, Wang M, Zhang L, Fu J, et al. Whole genome gene copy number profiling of gastric cancer identifies PAK1 and KRAS gene amplification as therapy targets. Genes Chromosomes Cancer. 2014;53:883–94. https://doi.org/10.1002/gcc.22196.
125. Roessler S, Jia H-L, Budhu A, Forgues M, Ye Q-H, Lee J-S, et al. A unique metastasis gene signature enables prediction of tumor relapse in early-stage hepatocellular carcinoma patients. Cancer Res. 2010;70:10202–12. https://doi.org/10.1158/0008-5472.CAN-10-2607.
126. Grinchuk OV, Yenamandra SP, Iyer R, Singh M, Lee HK, Lim KH, et al. Tumor-adjacent tissue co-expression profile analysis reveals pro-oncogenic ribosomal gene signature for prognosis of resectable hepatocellular carcinoma. Mol Oncol. 2018;12:89–113. https://doi.org/10.1002/1878-0261.12153.
127. Fujiwara N, Kubota N, Zhu S, Nakagawa S, Baba H, Hoshida Y. Disseminative recurrence signature for hepatocellular carcinoma from nonalcoholic fatty liver disease. Gastro Hep Adv. 2023;2:681–3. https://doi.org/10.1016/j.gastha.2023.03.021.
128. Ning J, Ye Y, Shen H, Zhang R, Li H, Song T, et al. Macrophage-coated tumor cluster aggravates hepatoma invasion and immunotherapy resistance via generating local immune deprivation. CR Med. Elsevier; 2024;5. https://doi.org/10.1016/j.xcrm.2024.101505. Cited 2024 May 28.
129. Cancer Genome Atlas Research Network, Ley TJ, Miller C, Ding L, Raphael BJ, Mungall AJ, et al. Genomic and epigenomic landscapes of adult de novo acute myeloid leukemia. N Engl J Med. 2013;368:2059–74. https://doi.org/10.1056/NEJMoa1301689
130. University X, Lin. UnionH: A Multi-Cohort Gastric Cancer Dataset for Transcriptomics and Proteomics Analysis. Datasets. https://doi.org/10.5281/zenodo.14864800(2025).

Publisher's Note